

RESEARCH ARTICLE

10.1029/2017JB015372

Special Section:

Stress at Active Plate Boundaries - Measurement and Analysis, and Implications for Seismic Hazard

This article is a companion to Liu et al. (2018), <https://doi.org/10.1029/2017JB015374>.

Key Points:

- New conceptual model for cratonic keel delamination-refertilized keel delaminates along a weak midlithospheric discontinuity layer (MLDL)
- Keel stability is closely related to the stability of the craton's surrounding lithosphere in the depth range of the MLDL
- Keel delamination appears to be supported by seismic observations beneath northern China and North America

Supporting Information:

- Supporting Information S1
- Movie S1
- Movie S2
- Movie S3
- Movie S4
- Movie S5
- Movie S6
- Movie S7
- Movie S8
- Movie S9
- Movie S10

Correspondence to:

L. Liu, J. P. Morgan, and Y. Xu,
liangliu@gig.ac.cn;
jason.morgan@rhul.ac.uk;
yigangxu@gig.ac.cn

Citation:

Liu, L., Morgan, J. P., Xu, Y., & Menzies, M. (2018). Craton destruction 1: Cratonic keel delamination along a weak midlithospheric discontinuity layer. *Journal of Geophysical Research: Solid Earth*, 123, 10,040–10,068. <https://doi.org/10.1029/2017JB015372>

Received 21 DEC 2017



Accepted 17 JUL 2018

Accepted article online 1 AUG 2018

Published online 8 NOV 2018

©2018. American Geophysical Union.
All Rights Reserved.

Craton Destruction 1: Cratonic Keel Delamination Along a Weak Midlithospheric Discontinuity Layer

Liang Liu^{1,2,3} , Jason P. Morgan^{2,4}, Yigang Xu¹ , and Martin Menzies^{1,2}

¹State Key Laboratory of Isotope Geochemistry, Guangzhou Institute of Geochemistry, Chinese Academy of Sciences, Guangzhou, China, ²Department of Earth Sciences, Royal Holloway University of London, Egham, UK, ³College of Earth Sciences, University of Chinese Academy of Sciences, Beijing, China, ⁴Department of Earth and Planetary Sciences, Harvard University, Cambridge, MA, USA

Abstract Cratons are generally observed to retain thick (>180 km) conductive keels for billions of years. However, some cratons have undergone keel removal, with well-documented examples being the eastern North China Craton (NCC) and the Wyoming Craton (WC). These keelless subregions appear to have kept a lithospheric bottom at ~80–100-km depths. This is also the depth range where modern cratons, including the remaining portions of the NCC and the WC, have seismically visible midlithospheric discontinuity layers (MLDLs). MLDLs are proposed to be regions of preferential accumulation of metasomatic minerals and/or anomalously wet (>1,000 ppm) peridotites, both of which would lead to a relatively weak rheology. We propose that the cratonic keels of the eastern NCC (ENCC) and the western WC (WWC) utilized this weak MLDL layer to delaminate from overlying lithosphere. We first explore this hypothesis with a lubrication-theory-based analytical model. This model suggests a close relationship between a cratonic keel's long-term stability and the strength of the MLDL's edge. We further test this prediction with less idealized 2-D numerical experiments which reveal that (a) dense lower keels beneath MLDL-bearing cratons can persist for billions of years as long as the MLDL's edges abut relatively cold and strong lithosphere; (b) MLDL edge failure can induce rapid intramantle lower keel delamination; and (c) the predicted rates of keel delamination along a ~10-km-thick MLDL with a hydrous olivine or metasomatic mineral-dominated rheology are consistent with observations for the removal speeds of the WWC and the ENCC.

1. Introduction

Cratons are extremely long-lived and extremely stable continental regions. Their tectonic quiescence has been attributed to their 150–220-km-thick lithosphere that contains a compositionally highly viscous and buoyant cratonic mantle keel (Jordan, 1988; Lenardic & Moresi, 1999; Menzies et al., 2007; Sleep, 2003). However, cratonic keel-removal events have been well documented for the Eastern North China Craton (ENCC; Griffin et al., 1998; Menzies et al., 1993; Xu, 2001; Xu et al., 2009; Zhu et al., 2012) and the Western Wyoming Craton (WWC; Egger & Furlong, 1991; Wu et al., 2014). Both events appear to be associated with subsequent large-scale crustal deformation (Feeley et al., 2002; Zhu et al., 2012) and magmatic flare-ups within 20 Myr (see Figure 1). Other more speculative examples of known keel removal events may include the Dharwar Craton and the Brazilian Craton (cf. Griffin, Kobussen, et al., 2009; Read et al., 2004; Wu et al., 2014). After keel removal events, former cratonic regions appear to retain relic lithospheric mantle to depths of ~80–100 km (see Figures 1 and 2b; cf. Hansen et al., 2015; Hopper et al., 2014; Wu et al., 2014; Zhang et al., 2008; Zheng et al., 2001; Zhu et al., 2012). This is directly documented by the presence of shallow (< approximately 80 km), but not deep (> approximately 80 km), Archaean mantle xenoliths in later magmatism (Menzies et al., 1993; Xu, 2001; Zheng et al., 2001).

During the long-term evolution of a craton, its overall mantle keel buoyancy can be affected by mantle refertilization processes (Gao et al., 2002; Griffin et al., 1998, 2004; O'Reilly & Griffin, 2013; Tang et al., 2013). As refertilized keel bases (cf. Griffin, O'Reilly, et al., 2009) or relatively *young* Proterozoic keel bases (ca. 1.8 Ga; Djomani et al., 2001; Gao et al., 2002) contain compositionally denser peridotites, they can sometimes have a 0.5–1.9% average compositional density decrease compared to the primitive mantle (Artemieva & Vinnik, 2016; Kaban et al., 2003, 2016; Lee, 2003; Lee et al., 2011; Mooney & Kaban, 2010). For cratons containing a fertile/refertilized keel base, the negative thermal buoyancy associated with a thick mantle keel can be larger than that of the positive *floating* tendency due to the keel's average

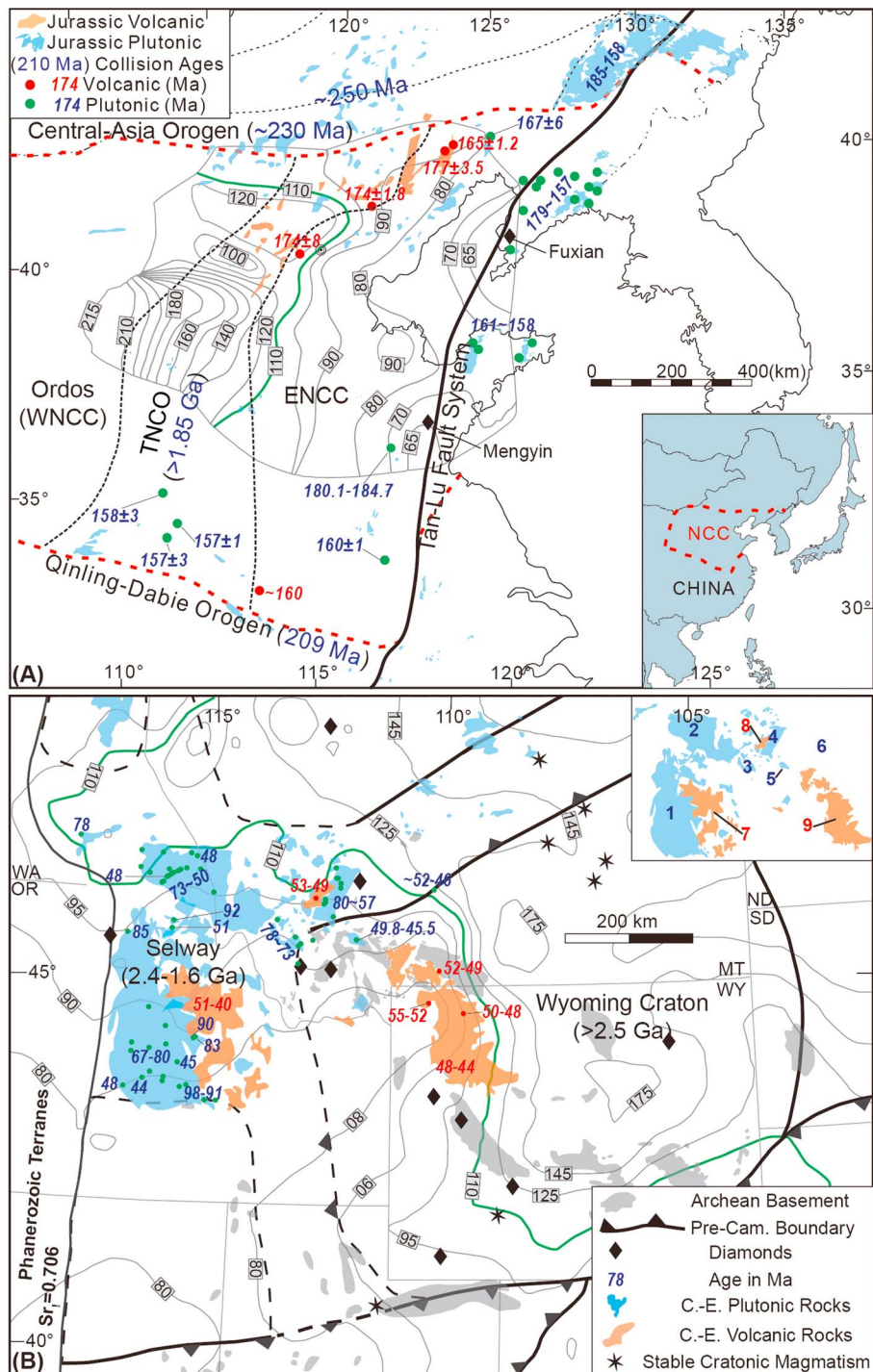


Figure 1. Geological and geophysical maps of the ENCC and the Western Wyoming Craton. (a) Eastern North China Craton (ENCC): Lithospheric thickness contours (in km) are from Zhu et al. (2012). Abbreviations: Western Northern China Carton (WNCC). Magmatism: (1) Tongshi (Lan et al., 2012), (2) Southern Hanjialing (Wu et al., 2005), (3) Xinglonggou (Yang & Li, 2008), (4) Tiaojishan (Davis et al., 2001), (5) Heigou (Wu et al., 2005), (6) Nandaling (Y. Zhao et al., 2006), (7) Lanqi (Yang & Li, 2008), (8) Xinyang (Zheng et al., 2008), (9) Jiaodong (Yang et al., 2012). (b) Western Wyoming Craton: Post-keel-removal magmatism is located on the Paleoproterozoic Selway terrane in its west (Foster et al., 2006). Because this terrane is known to contain Archean basement and diamond mines, the western limit to the paleoproterozoic Selway terrane in its west (Foster et al., 2006). Lithospheric thicknesses are converted from temperature contours at ~82-km depth (Hansen et al., 2015), under the assumption that the local geotherm is steady state (see supporting information S1). Abbreviation: C.-E. - Cretaceous to Eocene times. Labeled Magmatism (numbers in inset figure): (1) Atlanta (Gaschnig et al., 2010), (2) Bitterroot (Gaschnig et al., 2010), (3) Pioneer (Foster et al., 2012), (4) Boulder (Lund et al., 2002), (5) Tobacco (Mueller et al., 1996), (6) Crazy Mountain (Dudás, 1991), (7) Challis (Norman & Mertzman, 1991), (8) Lowland Creek (Dudás et al., 2010), (9) Absaroka (Feeley & Cosca, 2003).

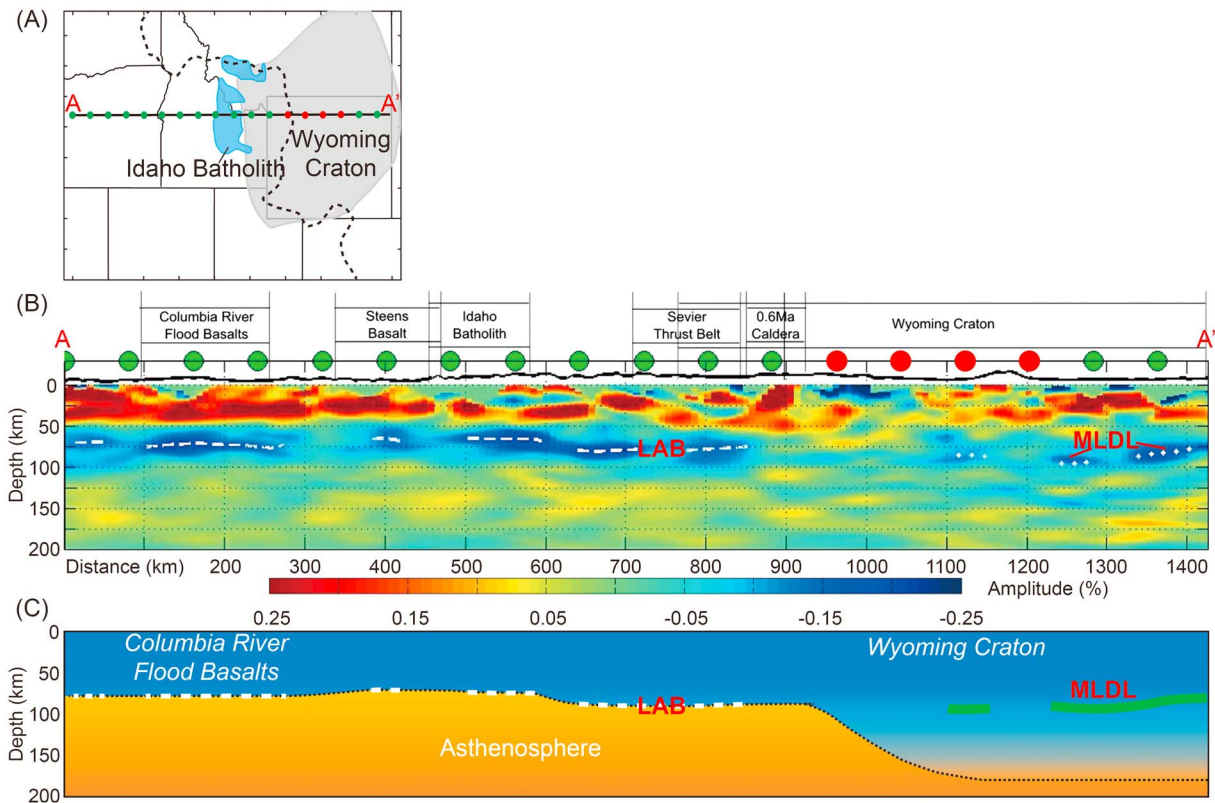


Figure 2. (a) Cross-section locations for the seismic structure in (b); the red dots mark the region of the Wyoming Craton beneath which the MLDL appears to be absent; the black-dashed line marks the contour of the estimated ~95-km-thick lithosphere in Figure 1. (b) Seismic structure of the northwestern United States (Hopper et al., 2014) along the profile shown in (a). The proposed lithosphere-asthenosphere boundary (LAB) is marked with a white-dashed line, while the MLDL is marked with white dots. The MLDL appears to be absent beneath the part of the Wyoming Craton where the region of significant lithospheric thinning terminates; (c) interpretation of (b). The present-day LAB beneath Selway Terrane and the Western Wyoming Craton (see Figure 1) shares a similar depth with the present-day MLDL in the un-thinned eastern Wyoming Craton. MLDL = midlithospheric discontinuity layer.

depletion being greater than that of the asthenosphere (see the numerical experiments in section 5.2; Kaban et al., 2003). In this case, the factors that resist the tendency of the denser keel to sink will be the overall buoyancy of its overlying continental crust and the strong mechanical strength of the lithosphere. If crust-mantle or intramantle coupling is disturbed, then cratons could experience keel-removal event(s) through lithospheric delamination (Bird, 1979; Kay & Kay, 1993). Continental delamination was originally proposed, with crust-mantle delamination, for the recent uplift of the Colorado Plateau (Bird, 1979). Its geochemical implications were first explored systematically by R. W. Kay and Kay (1993), who further emphasized the possibility that a lower crustal transformation to denser eclogite could be the driving force for delamination. However, as noted, above, there is strong observation evidence that shallow lithospheric mantle relics persist after cratonic keel removal events.

We propose that potential intracratonic decoupling occurs along a seismologically revealed intracratonic layer named the midlithospheric discontinuity (MLD) that is seen at ~80–100 km (Abt et al., 2010; Aulbach et al., 2017; Chen et al., 2014; Hopper et al., 2014; Nita et al., 2016; Selway et al., 2015; Sodoudi et al., 2013). The MLD is a common but not ubiquitous seismic feature in cratonic regions. Here we suggest that the MLD is better viewed as a thin layer instead of a discontinuity, for example, an MLD layer (MLDL). Since the MLD was identified, its potential origins have been widely discussed. Proposed mechanisms of formation include

1. A transition to grain boundary sliding due to the upper mantle under this region being richer in water (up to 1,000 ppm; Karato et al., 2015). Such high chemically bound water contents can also weaken its strength in dislocation and diffusion creep (Hirth & Kohlstedt, 2004; Korenaga & Karato, 2008). As potential evidence supporting this mechanism, the Cretaceous (~120 Ma) ENCC mantle has been identified to locally contain >1,000-ppm water (Xia et al., 2013).

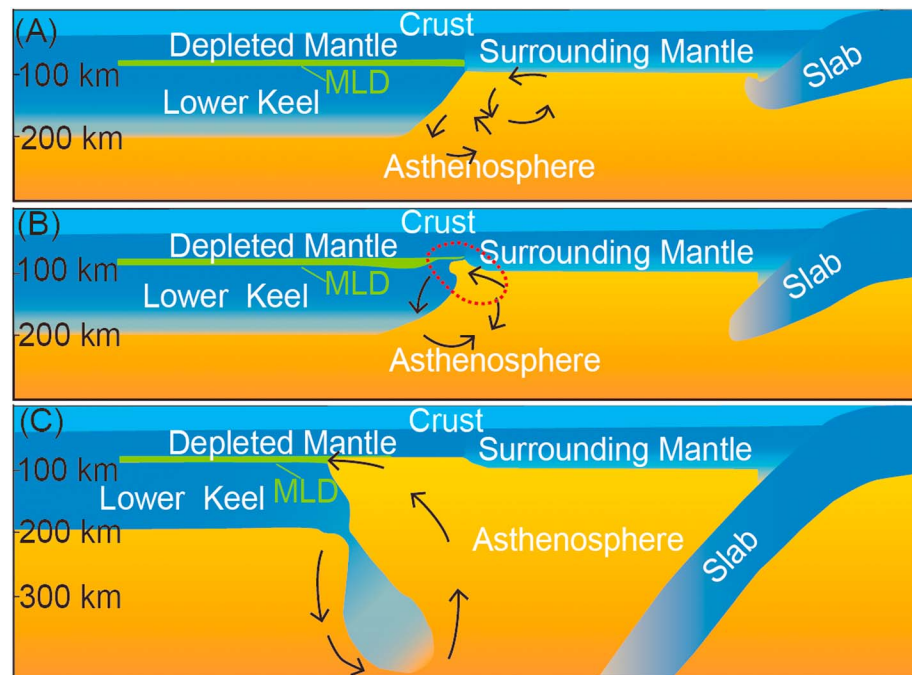


Figure 3. Intramantle keel tearing and delamination model. (a) Onset stage. Configuration at the onset of tearing after potential mechanisms discussed in section 6 has modified the craton's margin so that the MLDL is now *close* to margin's edge. (b) Initial tearing stage. The keel is denser than its adjacent asthenosphere. Now materials adjacent to the MLDL's edge are soft enough so that the denser keel can start to sag away from the MLDL. The keel's sagging induces a low-pressure zone within the MLDL (see Figures 4, 5 and 7), which acts to suck material within and along the MLDL toward the tip of the growing keel tear. This region of inward flow is marked by a red-dashed circle. Induced inward flow can further weaken inflowing material due to enhanced power-law creep. This effect will accelerate the keel's tearing along the MLDL. (c) Mature keel tearing stage. Once there is a good flow connection between the MLDL and its adjacent asthenosphere then relatively ductile asthenosphere can readily compensate the void left by keel tearing. This is the stage of most rapid keel delamination. MLDL = midlithospheric discontinuity layer.

2. Tectonic stacking. This can lead to an MLD if cratonic layers have sharp enough compositional differences (Abt et al., 2010). In this scenario, the interface between stacked layers would be rich in volatile-rich melts (Griffin et al., 2004) whose rheology could be similar to that of metasomatized mantle.
3. Metasomatic layers (Selway et al., 2015) deposited during multiple episodes of metasomatism (O'Reilly & Griffin, 2013). MLDLs appear to exist at a similar depth (80–100 km) to that proposed for enhanced metasomatism of cratonic lithosphere (cf. Griffin et al., 2003; Sodoudi et al., 2013). Metasomatic minerals, for example, mica and/amphibole, are found in mantle xenoliths in the ENCC, the WWC, Tanzanian Craton and South African craton (Dawson & Smith, 1988; Downes et al., 2004; Dudás, 1991; Gao et al., 2002; Griffin et al., 2004; Lu et al., 1991; Tang et al., 2013). These xenoliths are named MARID xenoliths, composed of Mica (>50 vol.%), Amphibole (~25 vol.%), Rutile, Ilmenite, and Diopside (Dawson & Smith, 1977). At 80–100-km depths, amphibole (Getsinger & Hirth, 2014) and mica (Kirby & Kronenberg, 1987) appear to be weaker than wet olivine (Hirth & Kohlstedt, 2004).

In summary, MLDLs, if due to any of the above mechanisms, are likely to have a relatively weak rheology in comparison to their overlying and underlying lithospheric mantle. We currently favor the third (metasomatic layer) hypothesis.

We propose that dense cratonic lower keels can delaminate along a weak intramantle MLDL and sink into deeper mantle (see Figures 2c and 3). Note that the exact thickness needed for a weak MLDL to have a significant dynamic impact is tightly linked to the viscosity reduction within this layer. Lubrication theory (see Section 3 below) indicates that the effective viscous strength of the layer will be proportional to its viscosity but inversely proportional to the cube of its thickness, for example, doubling the thickness of the MLDL would have the same effect as reducing its viscosity by a factor of 8. Top-side seismic reflection techniques suggest the topside wavespeed reduction in this layer is associated with a relatively sharp (<5 km thick) depth

interval and a total layer thickness of ~10–25 km (Karen Fischer, personal communication, to JM, November 30, 2017). Receiver function and SS-precursor-inferred layer thicknesses are consistent with a ~10-km-thick MLDL but have much cruder vertical resolution. For example, Sp receiver functions are consistent with inferred MLDL thickness in the western United States of 15–30 km (Lekić & Fischer, 2014), while SS-precursor measurements only constrain the *reflector* to be a “sharp discontinuity with an average velocity contrast of $5 \pm 1.5\%$ occurring over <14 km” (Tharimena et al., 2017). In what follows, we will usually assume that the main weak region of the MLDL is 10 km thick.

A consequence of this hypothesis is that the lithosphere-asthenosphere boundary (LAB) in regions that have undergone a keel delamination event should have a depth similar to that of the MLD in preserved cratonic keels, as is seen in the western United States (Figures 1 and 2b; Hopper et al., 2014). A similar depth relationship appears to also exist between the LAB in the keelless ENCC and the remaining MLDL beneath the unthinned western NCC (Chen et al., 2014).

Here we will further explore the dynamics of cratonic keel delamination along an ~80–100-km-deep MLDL (see Figure 3). We first review previous models for cratonic keel removal, which appear to have limitations in explaining some observations on the ENCC and WCC. Second, we discuss a lubrication-theory-based analytical analysis that provides insights into the mechanics of this keel delamination process. Third, we examine these predictions using less idealized 2-D numerical experiments.

2. Review of Previous Scenarios for Keel Removal

After it was recognized that the NCC had lost its cratonic keel (Menzies et al., 1993), many conceptual and numerical models were proposed to thin a keel. Most are related to convective erosion. However, these previous models appear to have limitations to explain some observations on the ENCC and the WCC.

2.1. Convective Erosion Models

Many scenarios propose that cratonic lithosphere can thin by convective erosion (Xu, 2001) driven by a Rayleigh-Taylor-type gravity instability (cf. Conrad & Molnar, 1997). These models share the assumption that the keel has lost its high strength before removal begins. Specific keel weakening mechanisms include

1. Keel heating and/or yielding during orogenic events (Conrad & Molnar, 1997; Gorczyk et al., 2012; Houseman et al., 1981);
2. Long-term (>1 Gyr) keel refertilization (Foley, 2008; O'Reilly & Griffin, 2013; Tang et al., 2013); and
3. Relatively rapid (<200 Myr) weakening due to the incorporation of volatiles from nearby subducting slabs (L. J. He, 2014; Niu, 2005; Wang et al., 2016; Wenker & Beaumont, 2017; D. P. Zhao, 2004).

These hypotheses all appear to conflict with some observations. Keel thinning driven by orogeny appears inconsistent with keel-removal events recorded in cratonic interiors (see Figure 1). Keel weakening due to long-lived keel refertilization appears inconsistent with the presence of sudden craton-wide magmatic flare-ups (see Figure 1). If keel thinning by long-term convective erosion was a general process, some modern cratons would be expected to exist in an intermediate state between stable and keelless, for example, to have a blob-like lithospheric base like that described in models of the growth of a Rayleigh-Taylor gravity instability (Conrad & Molnar, 1997; Houseman et al., 1981). This does not appear to be the case.

Given that both the ENCC and the WWC appear to have been adjacent to long-term active subduction zones (cf. Engebretson et al., 1985; Xu et al., 2009), a further puzzle exists in scenarios for slab-volatilization-induced weakening to remove cratonic keels: Why did on-cratonic magmatism (see Figure 1a) occur in the ENCC interior almost contemporaneously with the proposed initiation of subduction of the Pacific Plate (cf. 185 Ma; Maruyama et al., 1997; Wu et al., 2011), while WWC delamination occurred at least ~70 Myr after the initiation of subduction of Farallon Plate at approximately 150 Ma (Engebretson et al., 1985)? Why would not similar weakening mechanisms proceed along similar time scales?

2.2. Flat Subduction

Magmatic flare-ups have previously been described as a frequent by-product of flat subduction. This concept was developed to explain the Laramide Orogenic event in western North America (cf. English & Johnston, 2004; Snyder et al., 1976). In this scenario, spatially and temporally continuous magmatism would indicate transient slab positions during an episode of flat subduction.

However, the time-space patterns of on-craton Laramide magmatism appear inconsistent with predictions from simple scenarios for flat subduction. For example, Challis and Lowland Creek Volcanism (see magmatism 7 and 8 in Figure 1b) occurred later than the earliest events in the Absaroka Volcanism to the east (Feeley & Cosca, 2003) but earlier than the latest Absaroka events (see magmatism 9; Figure 1b). This pattern cannot be easily explained by eastward migrating flat subduction followed by westward slab rollback (Dudás, 1991). Furthermore, the temporal contiguity of the earliest magmatism on the northern subregion of the ENCC (see Figure 1a) would indicate a southward flat subduction migration. This also conflicts with the proposition that contemporary paleo-Pacific subduction initialized at ~190–180 Ma and was >800 km away from the sites of magmatism (cf. Maruyama et al., 1997; Wu et al., 2011).

Second, unlike subduction beneath thinner (e.g., 100 km) lithosphere, slab subduction beneath cratons (~200 km) is expected to be influenced by the thick keel (cf. Manea et al., 2012; Sigloch et al., 2008). Beneath a ~200-km-thick keel, a cold and volatile-stripped slab would not further dehydrate to generate large-scale on-craton magmatism (Dudás, 1991). Indeed, the current flat subduction beneath South America is associated with an absence of magmatism, not enhanced magmatism (Kay & Coira, 2009). Furthermore, if early on-craton mafic magmatism can document the transient lithospheric thickness during magmatism to be less than ~100 km (Dudás, 1991; Xu, 2001), then should not these magmas have preferentially sourced more volatile-rich slab components, instead of the magma-composition-inferred enriched lithospheric mantle source (Dudás, 1991; Feeley & Cosca, 2003; Menzies et al., 1993; Norman & Mertzman, 1991; Wu et al., 2005; Xu, 2001)? While flat subduction may be mechanically linked to episodes of cratonic keel thinning, thinning typically does not rapidly happen when a flat slab lies directly beneath a cratonic keel.

2.3. Lithospheric Delamination Along a Weakened Moho

As noted above, lithospheric mantle delamination has frequently been proposed to be the primary mechanism for the destruction and recycling of continental lithosphere (cf. Bird, 1979; Gao et al., 2002, 2009; Kay & Kay, 1993). Based on this conceptual model, many authors have described and studied scenarios in which a dense lithospheric root rapidly peels along the weak and/or deepened Moho (Bao et al., 2014; Bird, 1979; Gray & Pysklywec, 2012; Krystopowicz & Currie, 2013; Z. H. Li et al., 2016; Morency & Doin, 2004). Most of these studies highlight that the negative buoyancy of the lithospheric mantle is what triggers delamination, with possible additional contributions from an eclogitized lower crust. Some experiments (Morency & Doin, 2004) demonstrate that lower crustal eclogitization is not needed as long as the Moho is weak enough.

However, cratonic keel delamination from the Moho appears to conflict with several key observations on the ENCC and the WWC:

1. Relics of the ancient lithospheric mantle typically remain after a keel thinning event, as revealed by basalt-bearing xenoliths (cf. Dudás, 1991; Tang et al., 2013; Zhang et al., 2008; Zheng et al., 2001). This would be a geometric impossibility if delamination occurred along/above the Moho. Instead, this clearly suggests that at least a layer of former cratonic mantle survives after a keel delamination event. Similarly, a layer of relic shallow lithospheric mantle appears to survive after noncratonic delamination events such as that proposed to have recently happened beneath the Canadian Cordillera (Bao et al., 2014). After keel delamination there, ~1 Ga “old lithospheric mantle” xenoliths were exhumed, carried in postdelamination asthenosphere-sourced magmas (Francis et al., 2010; Peslier et al., 2000).
2. Regional keel thinning appears to be independent of lower crustal eclogitization. Until late Cretaceous times, ancient lower crust still existed beneath the ENCC (cf. Zhu et al., 2012), while contemporaneous large-scale mantle melting suggests that the craton had already been thinned to ~80 km (Xu et al., 2009).

In contrast to these previous models, keel delamination along an intracratonic MLDL (see Figure 3) appears to be able to simultaneously explain (1) the flare-up of magmatism on craton (see Figure 1); (2) the presence of relic ancient crust and shallow mantle in postdestruction lithosphere; and (3) the similar depth distribution of the postdelamination LAB and predelamination MLDLs (see Figure 3). To progress further in assessing this hypothesis, we explore this conceptual model with semianalytical and numerical modeling approaches.

3. Theoretical Analysis

3.1. Lubrication-Theory-Based Model

The feasibility and factors influencing the proposed scenario here for cratonic keel delamination can be explored using a simple lubrication-theory-based analytical model. As illustrated in Figure 4, the lower keel's decoupling from its overlying lithosphere is simplified to be a process of downward bending of denser keel root, with compensating material flowing into the delaminating region. This simplified model shares a lubrication-theory formulation with Bird's (1979) original delamination model. It primarily differs from Bird's model in that Bird imagined the weak channel to be hot, ductile, lower crust, while we propose that it takes place along a deeper weak MLDL. We also propose that the rate limiting factor is the ability of material to flow into the growing intralithospheric delamination channel. In contrast, Bird envisioned there was limitless easy supply of weak material by upwelling of asthenosphere through a vertical conduit within the lithosphere. Here the delaminating lower keel is assumed to be (a) overlain by a viscous conduit-like MLDL channel (see the yellow area in Figure 4) into which the material inflows allow keel separation; (b) embedded at its distal end (the left end in Figure 4), for example, where the MLDL disappears laterally; (c) subjected to a uniform body load (F) due to the average net density difference between the denser lower keel and its adjacent asthenosphere (see equation (1)).

The body load F that drives delamination is given by

$$F(x) = \overline{\Delta\rho}gK(x), \quad (1)$$

where $K(x)$ is the lower keel thickness as a function of lateral distance x , $\Delta\rho$ is the average density difference between the lower keel and adjacent asthenosphere, and g is the gravitational acceleration.

As the lower keel flexes and delaminates (the lower keel is the black-dashed line in Figure 4), the vertical deflection of the plate ω from its initial position is given by equation (2) (Turcotte & Schubert, 2014), where the flexural rigidity $D = Eh^3/12(1 - \nu^2)$ and L are the lateral distance over which delamination has occurred:

$$\omega_1 = \frac{Fx^2}{D} \left(\frac{x^2}{24} + \frac{Lx}{6} + \frac{L^2}{4} \right). \quad (2)$$

For an increment δL of propagation of the delaminating region (the plate is the blue-dashed line in Figure 4), the new ω would be

$$\omega_2 = \frac{F(x + \delta L)^2}{D} \left(\frac{(x + \delta L)^2}{24} + \frac{(L + \delta L)(x + \delta L)}{6} + \frac{(L + \delta L)^2}{4} \right). \quad (3)$$

With terms containing δL^2 and higher orders neglected, the incremental deflection $\delta\omega$ for an increment δL of delamination is given by

$$\delta\omega = \omega_2 - \omega_1 = \delta L \left(\frac{F}{D} \right) \left(\frac{x^3}{3} + x^2L + \frac{xL^2}{2} \right). \quad (4)$$

This increment of keel bending would leave a material void (see Figure 4), to be filled by lateral flow within the weak MLDL channel. The area (e.g., volume per unit cross section) of this material hole ΔS is given by

$$\Delta S = \int_0^x \delta\omega(x) dx = \delta L \left(\frac{F}{D} \right) \left(\frac{x^4}{12} + \frac{x^3L}{3} + \frac{x^2L^2}{4} \right). \quad (5)$$

In order for the lower keel to sag further, material must flow into the MLDL to compensate the void space ΔS . This flow Q is

$$Q(x) = v \left(\frac{F}{D} \right) \left(\frac{x^4}{12} + \frac{x^3L}{3} + \frac{x^2L^2}{4} \right), \quad (6)$$

where the speed of delamination $v = \delta L/\delta t$.

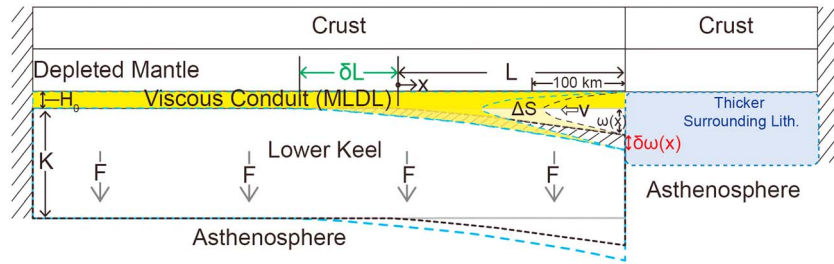


Figure 4. Lubrication-theory based analytical model. If the net density (compositional + thermal) of the lower keel is higher than that of the adjacent asthenosphere ($F > 0$), the lower keel will tend to sag downward along the weak MLDL. Sagging of the lower keel cannot occur unless the material void (ΔS) is filled. If weak enough material can flow to fill this space, then rapid keel delamination can develop. Otherwise, the lower keel will not delaminate. X = horizontal distance; F = body force favoring keel sinking; H_0 = initial thickness of the weak MLDL; L = Length of keel tearing along the MLDL; δL = new increment of MLDL tearing; v = speed of lateral flow into and within the MLDL; $w(x)$ = additional opening of the MLDL as keel tearing develops; Lith. = lithosphere; MLDL = midlithospheric discontinuity layer.

In the lubrication theory approximation (cf. Batchelor, 2000; Bird, 1979; Parmentier & Forsyth, 1985), the pressure gradient dP/dx is related to flow $Q(x)$ by

$$\frac{dP}{dx} = -\frac{12\mu(x)Q(x)}{h(x)^3}, \quad (7)$$

where $\mu(x)$ is the MLDL channel viscosity at distance x . (This expression neglects buoyancy effects because the flow is assumed to be horizontal.)

In this case, the pressure reduction ΔP at a distance x is

$$\Delta P(x) = -12 \int_x^L \frac{\mu(x)Q(x)}{h(x)^3} dx. \quad (8)$$

The negative sign implies a pressure drop toward the tip of the laterally migrating region of delamination. If we assume that the total pressure drop dynamically balances the weight of the lower keel (F), then by equating equation (8) with equation (1), the growth rate of the delaminating region can be estimated from

$$\int_0^L \Delta P(x) dx = FL. \quad (9)$$

As the left-hand side of the equation (9) is difficult to integrate analytically, we numerically evaluate it in MATLAB, with a discrete sampling interval $\Delta x = 100$ m. If the MLDL viscosity $\mu(x)$ is assumed to be piecewise constant, $\int_0^L \Delta P(x) dx$ can be approximated by equation (10).

$$\int_0^L \Delta P(x) dx \approx \sum_{k=1}^n \overline{\Delta P(x_k)} \cdot \Delta x, \quad (10)$$

where $\overline{\Delta P(x_k)} = (\Delta P(x_{k-1}) + \Delta P(x_k))/2$, $n = L/\Delta x$, x_k is the coordinate of the k th grid point, and x_{k-1} is that of the previous grid point (for $k = 1$, $x_{k-1} = x_k$).

3.2. Analytical Model Results

Once the conduit flow velocity (v) is calculated, the tearing speed of keel delamination can be determined. This speed is a function of the channel's thickness (H_0), length (L), viscosity ($\mu(x)$), and of the negative buoyancy of the lower keel (F).

The effects of varying H_0 , F , and $\mu(x)$ are illustrated in Figure 5. Here we consider two scenarios: (1) the conduit viscosity is a constant; (2) the outermost 100 km of the conduit is stronger than the rest of the channel, which resembles a scenario where the layer and its underlying lower keel are strongly coupled with stronger surrounding mantle (see Figure 4). Here the stronger mantle should be treated as part of the tearing-linked conduit. In each plot, we only vary two variables while keeping the others constant.

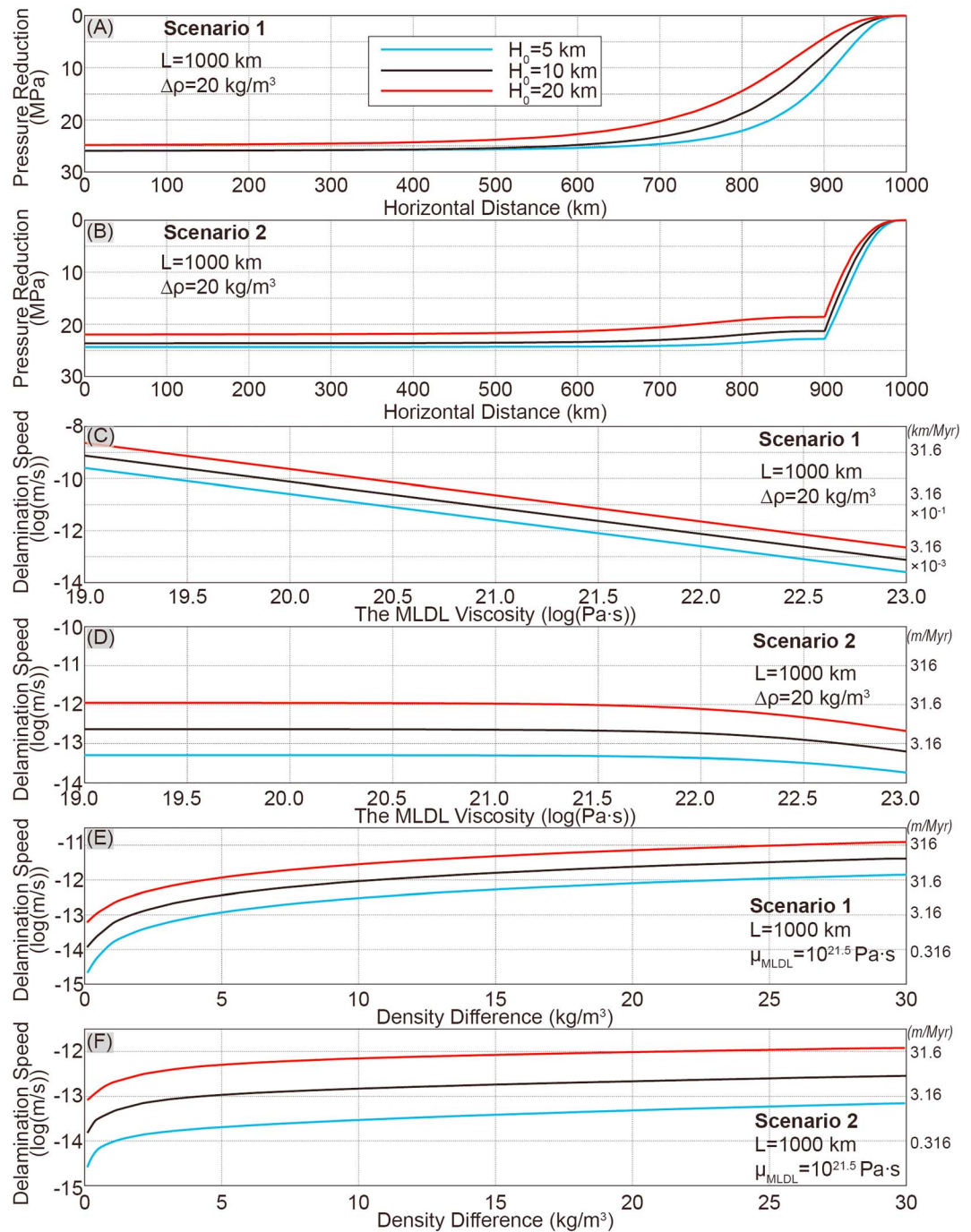


Figure 5. Effects of MLDL viscosity and keel density on mean conduit flow velocity (=speed of keel delamination). In (a)–(b), the pressure drop induced by keel sagging is plotted along the conduit (1,000 km marks the right end, see Figure 4). (c)–(d) the effects of MLDL viscosity on mean conduit flow velocity. (e)–(f) the effects of keel density on mean conduit flow velocity. μ_{MLDL} = MLDL viscosity. $\Delta\rho$ = average net density difference between the keel and its neighboring asthenosphere. Note that the units (km/Myr) for the right axis of (c) differ from those (m/Myr) used for (d)–(f). MLDL = midlithospheric discontinuity layer.

In scenario 1 (see Figure 5a), the pressure (ΔP) within the conduit decays gradually in the first 250–300 km close to the outside (right) edge, where is also the range that the pressure gradient exists. In scenario 2 with a sharper outer edge (see Figure 5b), a significant pressure gradient only exists within the 100 km outermost edge of the conduit. In this scenario, conduit flow only occurs when the outermost region can deform enough to supply material into the weaker central portion of the MLDL’s low viscosity channel.

The speed at which the delamination tear migrates along the MLDL is controlled by the MLDL's viscosity in scenario 1. In scenario 2, it is controlled by the viscosity of the stronger *asthenosphere* and lithosphere that must also deform to supply material for the tear to propagate (see Figure 5d). Faster conduit flow and tearing happen when the density difference $\Delta\rho$ between the lower keel and adjacent asthenosphere is larger (see Figures 5e and 5f) or when the conduit is thicker (see Figures 5c–5f).

3.3. Implications

Based on the above analysis, two end-member situations for keel evolution will naturally arise.

If a MLDL channel ends within strong ($\sim 10^{23}$ Pa-s) surrounding mantle, then delamination will not happen. For these parameters, the tearing speed is estimated to be < 6 km/Gyr, for example, be essentially stable (see Figures 5d and 5f).

On the other hand, if the edges of an ~ 10 -km-thick weak MLDL are reactivated to have an $\sim 10^{19}$ -Pa-s viscosity (e.g., see Figure 10f), and this layer is underlain by a lower keel possessing a large enough net density difference (e.g., ~ 20 kg/m³, e.g., see the density panel in Figure 7a), the tearing speed is predicted to be > 30 km/Myr (see Figure 5c). In this scenario, a > 400 -km regional keel-removal event would happen within 15 Myr.

The change in delamination speed due to variations in layer thickness can be crudely estimated from the results in Figure 5c, which indicate that a 2 times thicker/thinner layer can lead to ~ 3.2 times faster/slower delamination speeds. Finally, although this model is only 2-D, the basic mechanics are also only 2-D, for example, flow along a weak intracratonic channel fed from the edge of the channel. Therefore, 3-D analysis is not needed to understand the basic speed and stresses/relief associated with this mode of intracratonic keel delamination.

4. 2-D Numerical Experiments

To further explore this scenario under less idealized conditions, we have also analyzed 2-D numerical experiments of this process.

4.1. Methods

The numerical experiments performed here use a modified version of 2-D incompressible elastoviscoplastic thermomechanical Lagrangian finite element code with diffusion and dislocation creep, “m2tri_trunk” (Hasenclever, 2010; Hasenclever et al., 2011). This version includes a free surface boundary condition (Andrés-Martínez et al., 2015). Melting is also included. Tracer particles are added for tracking different material properties. The 2-D experimental domain is subdivided using an adaptive triangle mesh generator that keeps high resolution across material boundaries and interfaces, for example, slabs and keels (see Appendix B). More details on the numerical approach are given in Appendices and in Andrés-Martínez et al. (2015), Hasenclever (2010), and Hasenclever et al. (2011). Table 1 shows the parameters used in numerical experiments.

4.2. Initial Density and Viscosity Structure and Boundary Conditions

We assume that mantle metasomatism (cf. O'Reilly et al., 2001; Tang et al., 2013) have increased the compositional keel density below the weak MLDL. This metasomatism would transform the keel from highly refractory peridotite (3,310 kg/m³ compositional density) to a compositional density of 3,340 kg/m³, a value still less dense than fertile asthenosphere (3,360 kg/m³; cf. Djomani et al., 2001; Griffin et al., 1999). These density parameters are crudely consistent with studies of kimberlite-borne mantle xenoliths (cf. Djomani et al., 2001; Griffin et al., 1999) and with craton gravity anomalies (Kaban et al., 2003). Intralithospheric MLDL material is prescribed to be even more buoyant, for example, set to the 3,320 kg/m³ compositional density found in amphibole-bearing mantle xenoliths (Dawson & Smith, 1988).

The side and lower boundaries of the box are set to be free-slip (see Figure 6a). In runs 2–7, stresses from a developing subduction slab are generated by imposing *plate subduction* geometry and velocities on the far edge beyond where the craton abuts a newly formed marginal rift basin (see Figure 6a). In run 1 (the case with a stable craton), the 200–350-km depth range of the right boundary segment is prescribed with a

Table 1
Parameters for Numerical Experiments

	A.M.	D.M.	L. Keel	S.M.	Slab	Crust	MLDL
Flow law parameters ^{a-g}							
A_{dis} (Pa ⁻ⁿ ·s ⁻¹)	10 ^{-15.05}	4.85·10 ⁻¹⁷			3.0·10 ⁻²²	1.4·10 ^{-21.2}	10 ^{-15.4}
n_{dis}	3.5					4.2	3
E_{dis} (kJ/mol)	480	535			540	445	356
V_{dis} (cm ³ /mol)				8			
A_{dif} (Pa ⁻ⁿ ·s ⁻¹)	10 ^{-8.65}					10 ^{-13.3}	10 ^{-13.3}
n_{dif}				1			
E_{dif} (kJ/mol)	335	375				170	170
V_{dif} (cm ³ /mol)				4			
r	$r_{dif} = 1.93, r_{dis} = 1.95$					-	-
Thermal parameters ^{h,k}							
G (GPa)			74			40	74
k (Wm/K)			3.3			2.5	3.3
H_r (μW/m ³)			0.033			0.25	0.33
c_p (J/(kg·K))				1,200			
T_0^m (°C)	1,081	1,136				-	1,081
$(\partial T^m / \partial f)_p$			132			-	132
$(\partial T^m / \partial P)_f$			250			-	250
Q_L (kJ/kg)			400			-	400
Density parameters ^{ij}							
ρ_0 (g/cm ³)	3.36	3.31	3.34	3.31	3.31	2.80	3.32
a_1 (10 ⁻⁴)	0.2697	0.27165	0.27165	0.27014	0.27768	0.27014	0.2697
a_2 (10 ⁻⁸ K ⁻¹)	1.0192	1.04971	1.04971	1.05945	0.95451	1.05945	1.0192
a_3 (K ²)	-0.1282	-0.15031	-0.15031	-0.1243	-0.12404	-0.1243	-0.1282
K (Gpa ⁻¹)	134	129	129	130	128	63	134

Note. Rheology parameters for the MLDL are varied in different experiments (see section 5 and Table 2). Parameters in this table are for a wet anorthite rheology (reference 5), the parameters for wet olivine and mica rheologies are from references 1, 7, and 6 below. Dislocation and diffusion viscosities are calculated using $\eta = 1/2A^{-1/n}C_{OH}^{-r/n}\epsilon_{ij}^{1/n-1} \exp((E + P \cdot V)/nRT)$, where η is viscosity, ϵ is the second invariant of strain rate, A is a preexponential constant, E is the activation energy, C_{OH} is water content in ppm H/Si (for olivine Fo90: 1 ppm H₂O = 16.35H/10⁶Si); r describes the exponential dependence of viscosity on water content, R is the universal gas constant, T is temperature, P is pressure, and V is activation volume. Subscript *dis* refers to parameters for dislocation creep, while *dif* refers to diffusion creep.

G = shear modulus; k = thermal conductivity; H_r = radioactive heat production; c_p = heat capacity; T_0^m = the solidus at room temperature and pressure; $(\partial T^m / \partial f)_p$ = the solidus's dependence on degree of melting; $(\partial T^m / \partial P)_f$ = the solidus's dependence on pressure; Q_L = Latent heat; ρ_0 = the reference density at room temperature (20 °C) and pressure (0.1 MPa); K = bulk modulus.

A.M. = asthenosphere, D.M. = cratonic lithospheric mantle above the MLDL, L. Keel = lower keel, cratonic lithospheric mantle below the MLDL, S.M. = noncratonic continental lithospheric mantle; MLDL = midlithospheric discontinuity layer.

^aHirth and Kohlstedt (2004). ^bHirth and Kohlstedt (1995). ^cKarato and Wu (1993). ^dWilks and Carter (1990). ^eRybacki and Dresen (2004). ^fKirby and Kronenberg (1987). ^gKorenaga and Karato (2008). ^hBrune et al. (2014). ⁱDjoman et al. (2001). ^jSchutt and Leshner (2006). ^kMorgan (2001).

~3 cm/year downward velocity for 10 Ma every other 100 Ma to simulate the effects of episodic subduction initialization.

As noted in section 1, because poor seismic resolution may lead to overestimates of MLDL thicknesses, in each experiment, the weak layer is assumed to be 10 km thick. Keel delamination rate is found to depend on the density contrast of the lower keel, MLDL rheology, and MLDL thickness (see Figure 5). Here we usually choose to fix the MLDL thickness to be 10 km in order to focus on exploring the effects of its rheology. The change in delamination speed due to differences in MLDL layer thickness can be crudely estimated from the results in Figure 5c, which indicate that a 2 times thicker/thinner layer can lead to ~3.2 times faster/slower delamination speeds.

4.3. Goals of the Numerical Experiments

Run 1 (see Table 2) is designed to test the first implication in section 3.3 that a dense lower keel beneath a weak MLDL can remain stable for >1 Ga, as long as the lithosphere adjacent to the weak layer remains strong. In this experiment, the lithosphere near the MLDL is 140 km thick, in which case its cooler geotherm implies that the lithosphere adjacent to the MLDL has >10²²-Pa·s viscosity (see Figure 7b). A

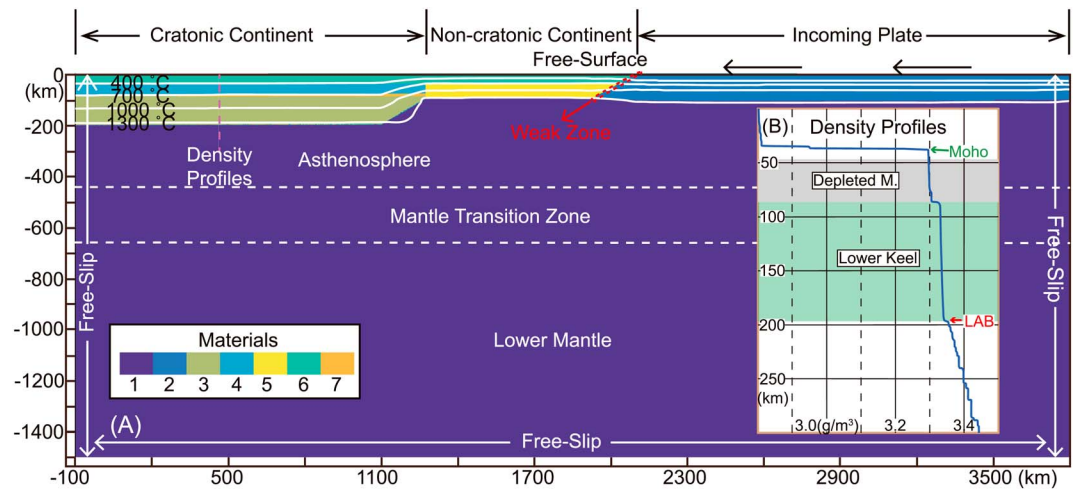


Figure 6. (a) The computational domain for runs 2–7. The region is 3,900 km wide \times 1,500 km deep. For runs 1, 4*, and 7*, it is 1,900 km wide \times 800 km deep. Mesh resolution for the midlithospheric discontinuity layer phase boundaries is \sim 450 m. Mesh resolution close to other phase boundaries (\sim 4.5 km) is about 10 times finer than that (\sim 45 km) in regions far away from these boundaries. Mesh resolutions within transitional distance range (\sim 210 km) are linearly interpolated between these end-member values. To simulate the far-field effects of subduction in runs 2–7, a leftward 2×10^{-9} m/s (\sim 6 cm/year) velocity is applied to represent the incoming plate. A <10 -km-thick weak zone (10^{19} Pa-s) is added between the oceanic plate and the continental plate to promote decoupling. Material types: (1) Asthenosphere, (2) oceanic plate, (3) cratonic keel, (4) depleted cratonic mantle, (5) noncratonic mantle, (6) crust, and (7) the midlithospheric discontinuity layer metasome. (b) Initial density structures with data from the profile marked by the purple dashed line in (a). M. = mantle; LAB = lithosphere-asthenosphere boundary.

gradual lithospheric thickness change close to cratonic edges is consistent with seismic observations (cf. Begg et al., 2009).

Because the rheology for the MLDL is quite uncertain, the experiments explore the implications for a wide range of MLDL rheologies that include a MARID-like mineral assemblage (Run 2), wet olivine (runs 4 and 4*), and the rheology of the mixture of MARID and wet olivine (runs 1, 3, 5, 6, 7, and 7*).

To crudely study the effects of nearby subduction process, runs 4 and 4* and runs 7 and 7* are compared to study scenarios with/without the subduction stress field.

Table 2
The Numerical Experiments Discussed in This Study

	Sub. F.	N.L.T.	MLDL rheology	Water on melting
Run 1	Yes	140 km	80% Wet Ol (214) + 20% Wet An	No
Run 2	Yes	100 km	Wet An	No
Run 3	Yes	100 km	33.3% Wet An + 66.6% Mica	No
Run 4	Yes	100 km	Wet Ol (214)	No
Run 4*	No	100 km	Wet Ol (214)	No
Run 5	Yes	100 km	90% Wet Ol (214) + 10% Wet An	No
Run 6	Yes	100 km	80% Wet Ol (214) + 20% Wet An	No
Run 7	Yes	100 km	80% Wet Ol (214) + 20% Wet An	Yes
Run 7*	No	100 km	80% Wet Ol (214) + 20% Wet An	Yes

Note. Effect of water on melting: in experiments where the MLDL is assumed to be mainly composed of wet peridotite (1,000-ppm water), water's extra effect on mantle melting is treated using equation (A15). The (214) marks the water content in ppm (by weight) used for calculating the rheology of olivine (see captions below Table 1). The 33.3% refers to the lithology's volume proportion used in equation (11). Sub. = subduction stress field, N.L.T. = noncratonic lithospheric thickness, Ol. = olivine, An. = anorthite; MLDL = midlithospheric discontinuity layer.

5. 2-D Numerical Results

The 2-D numerical experiments focus on exploring: (1) What parameters lead to the general *typical* situation of a stable long-lived keel; (2) What MLDL rheology is needed in order for a rapid delamination event to occur; (3) Which parameters lead to the *best simulating* numerical results when compared to the observations for partial keel delamination beneath the ENCC and the WWC; and (4) How do lateral variations in the MLDL and variations in far-field subduction potentially influence keel delamination?

The detailed keel delamination process will only be described for run 2. Other experiments with delamination evolve in similar patterns with varying speeds of keel tearing and delamination. Before discussing delamination experiments, we first examine the most common case in which a cratonic keel remains stable and does not delaminate over billions of years.

5.1. A Cratonic Keel Will Be Stable as Long as the MLDL's Edge Remains Stable

Cratonic keel removal is a rare geological phenomenon. Any keel delamination mechanism that can explain how keel removal happened in the ENCC and the WWC must first be able to explain the longevity of stable cratons.

The previous analysis suggests that stable cratonic keels should have margins where MLDLs abut relatively thick and strong surrounding lithosphere. If this geometry persists, the analytical analysis and numerical experiments both predict that a dense cratonic keel can stably exist over billions of years (see section 3.3). In the numerical example shown in run 1, the craton-edge lithospheric thickness (see Figure 7) is set to be 140 km, 40 km thicker than in the following experiments in which delamination happens. Other parameters and boundary conditions are similar to run 6 (see Table 2 and section 5.2), where the experiment has an ENCC-like keel delamination duration. After 1 Gyr of model time, the shape of the keel margin has become smoother. But the MLDL's shape change is hardly distinguishable (see Figure 7b), and the keel has remained stable.

To better understand when keels are stable/unable to delaminate, in Figure 7, the pressure variations in runs 1 and 4 (see section 5.2) are compared. Even though the keel delamination process in run 4 is the slowest shown here (see Figure 9), the theoretically predicted low pressure zone (see Figure 5a) can still be seen within the unreactivated portion of the MLDL (see pressure panel in Figure 7a), suggesting that the channel-flow mode of keel tearing is taking place. Over time, the power law creep associated with channel flow (see viscosity panel in Figure 7a) further weakens the surrounding mantle, which then more easily fills the void along the MLDL and accelerates keel tearing (see more details in section 5.2). In contrast, in run 1, because the MLDL edge is coupled to a stronger surrounding lithosphere, channel flow and its induced pressure drop do not appear within the MLDL (Figure 7b). Therefore, MLDL edge failure by tearing and delamination also does not occur. The cratonic keel can remain stable for billions of years, even with a prominent MLDL within it, as long as the MLDL-containing portions abut against strong surrounding lithospheric mantle.

5.2. Keel Delamination Experiments

In the following numerical experiments, we assume that a MLDL has developed to extend close to the edge of a cratonic keel. This scenario may have existed, for the ENCC and WWC, just after the cratons amalgamated with a recently formed *oceanic* plate, for example, the north-eastern China blocks (Wu et al., 2011) or accreted oceanic terranes to the west of the Salmon River suture zone (Foster et al., 2006).

5.2.1. Delamination Along a MLDL Linked to Mantle Metasomatism

In run 2, the MLDL is assumed to be related to persistent metasomatism events (see section 1). Although the rheology of mica has not been studied under mantle conditions, limited experiments suggest that it has a weaker rheology than amphibole, which in turn resembles that of wet anorthite (Getsinger & Hirth, 2014). We therefore use a wet anorthite rheology as the upper-limit strength for the rheology of a spatially discontinuous MARID-like MLDL.

Since horizontal temperature perturbations exist close to the keel, small-scale convection before delamination only occurs within the asthenosphere. The convection can further weaken the asthenosphere due to its power-law viscosity. But a weak asthenosphere alone does not affect keel stability unless the asthenosphere can break a mechanical connection to the MLDL. Because the keel margin is

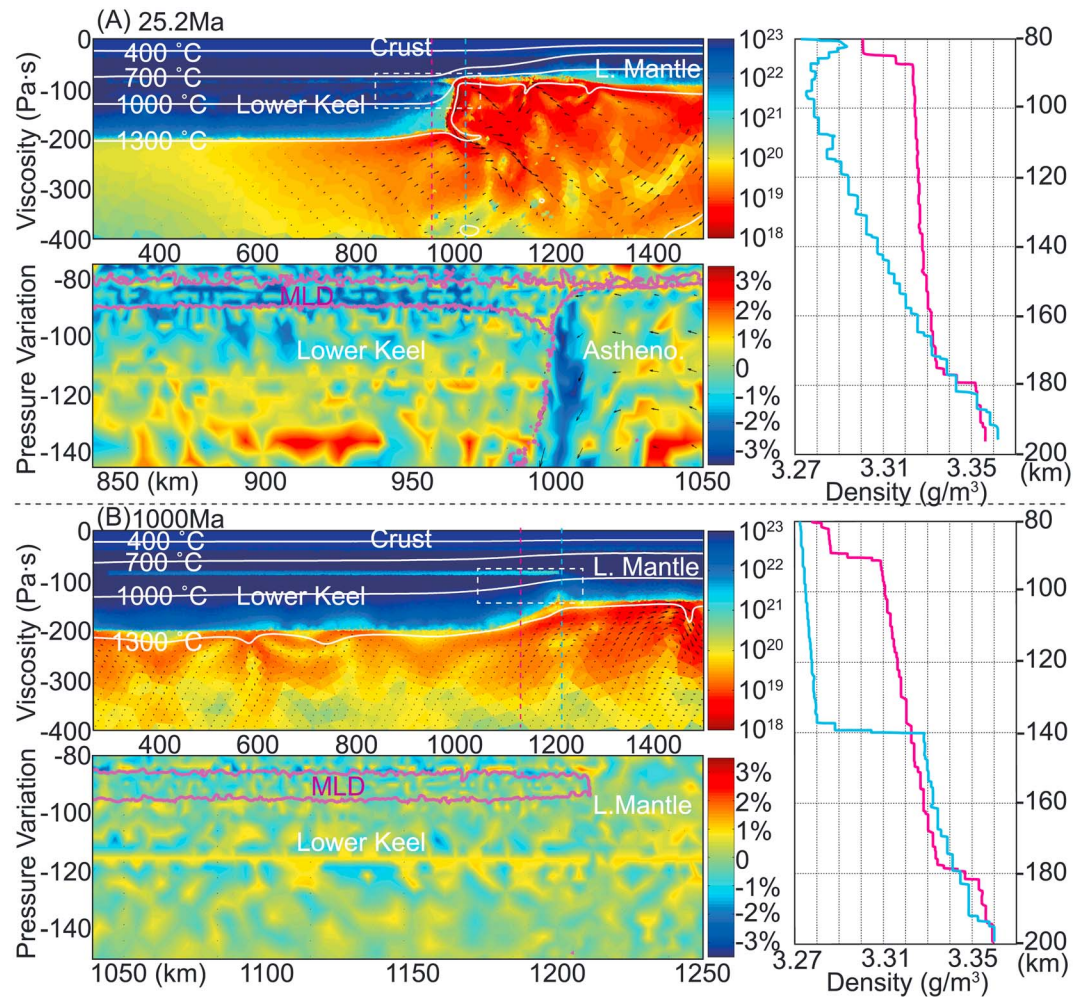


Figure 7. The low-pressure zone induced by partial keel tearing. (a) (lhs) Viscosity panel: viscosity plot during run 4. Pressure panel: pressure variations (P_{var}) within the dashed box shown in the viscosity panel. Pressure variations are shown in percent, where $P_{var} = (P - P_{ref})/P_{ref}$. The reference pressure profile P_{ref} is along the cyan-dashed line in the viscosity panel. (rhs) Density panel: density profiles along the vertical purple- and cyan-dashed lines shown in the same color in the viscosity panel. (b) Results after 1 Ga of evolution in run 1. No keel tearing is observed. The same plot conventions are used as in (a).

denser than the asthenosphere to its side (see density panel in Figure 8a), according to the analytical analysis in section 3, the lower keel should tend to sag downward as long as material can flow laterally into the weak MLDL. When the surrounding lithosphere mantle is both thin (100 km) and weak, then this mode of deformation can occur. As the keel margin sags downward, *intrachannel* material connecting the MLDL to the asthenosphere is pulled toward the MLDL (see material panel in Figure 8a and also Figures 10b–10d). The MLDL will have a direct horizontal connection with the asthenosphere once this stronger nonasthenospheric material is removed. When the direct connection forms, the rate of keel tearing increases (see Figure 8b). As it tears away and delaminates, the lower keel itself tends to break into ~300-km-wide blocks (see Figures 8b and 8c), with keel fragmentation events associated with temporary pauses in keel tearing. The denser keel relics sink, with overall asthenosphere cooling around the descending keel fragments (see material panel in Figure 8b). Some weak MLDL material is entrained into the deeper mantle during descent of delaminated keel fragments (see phase panel in Figure 8d). Due to its compositional buoyancy and weak rheology, most MLDL material either remains beneath the overlying relic lithosphere or is mixed into the asthenosphere (see material panel Figure 8c). Note that small-scale convection and

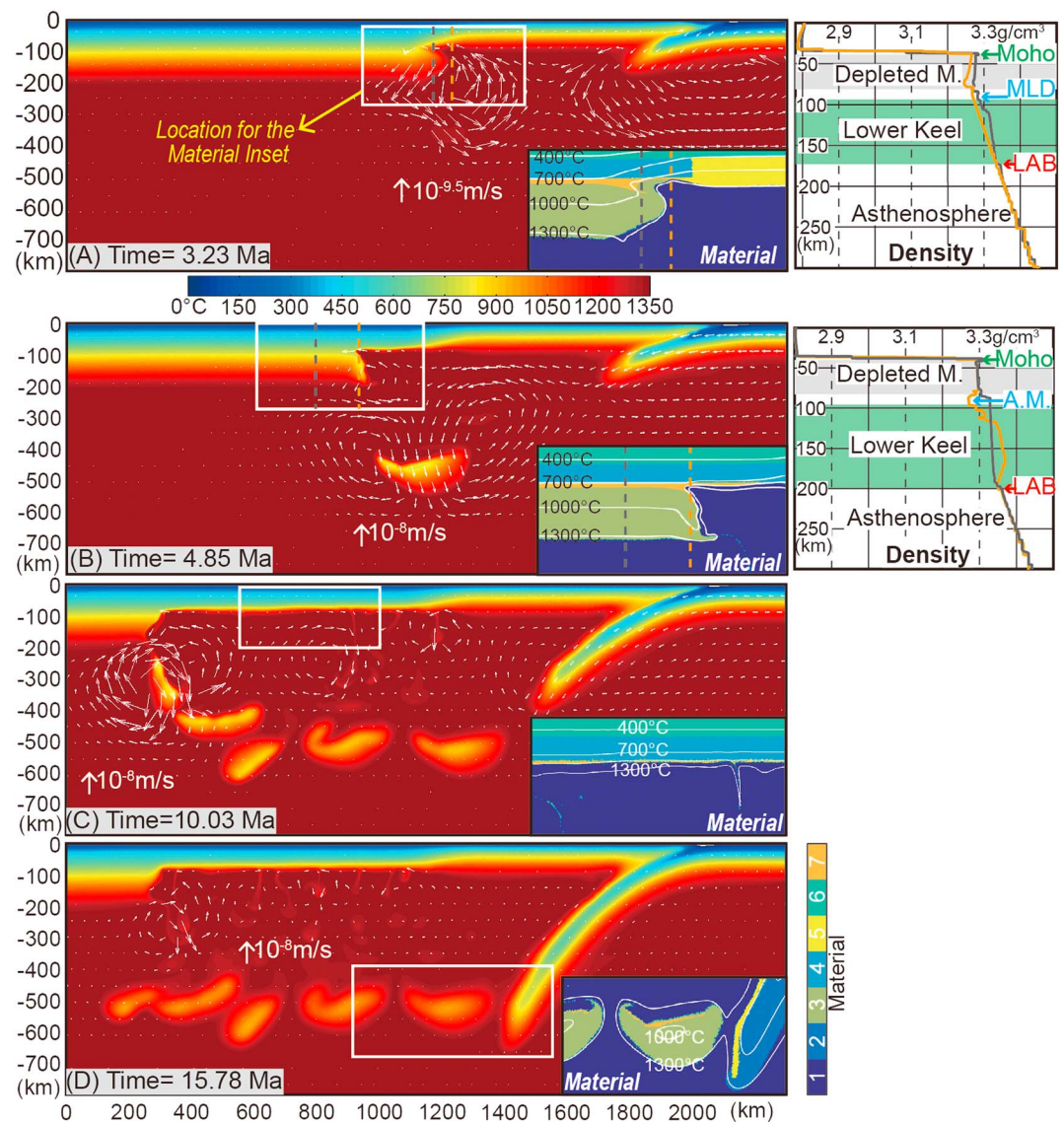


Figure 8. Numerical realization of the keel delamination process (results of run 2). (a) Keel starts to decouple from the MLDL. Material panel inset: material distribution within the white rectangle in (a). Density panel: density profiles along corresponding vertical-dashed lines with the same orange and brown colors in (a). Short white lines with arrow mark the direction of local convection. (b) The delaminating keel triggers vigorous convection. (c) The last keel fragment separates. Post keel-delamination evolution, for example, thermo-mechanical erosion, starts to develop in hotter relic regions. (d) Keel delamination stops where the MLDL terminates. Plot conventions are the same as in Figure 6. A. M. = asthenosphere; MLDL = midlithospheric discontinuity layer; LAB = lithosphere-asthenosphere boundary. Materials: 1-asthenosphere, 2-oceanic plate, 3-cratonic keel, 4-depleted cratonic mantle, 5 non-cratonic mantle, 6-crust, 7-the MLDL metasome.

deformation of the now-exposed lithosphere above the MLDL following a delamination event (Liu et al., 2016; see material panel; Figure 8c) will be the focus of a companion paper (Liu et al., 2018, which we will hereafter refer to as paper 2). Keel delamination stops in places where the intracratonic MLDL does not exist. In this scenario, the observed locally discontinuous nature of MLDLs (Chen et al., 2014; Hopper et al., 2014) is what limits the spatial scale of each regional keel delamination event. Note that intercratonic orogenesis and melting can also lead to melt-extraction-related removal of MLDL material.

Run 3 is a similar experiment to run 2. In this case, a mica plus amphibole rheology is considered as the weak-limit estimate to the strength of the MLDL. The MLDL's effective viscosity (μ_{MLDL}) is calculated assuming the bulk rheology given in equation (11), where x_1 is the volume proportion of amphibole.

$$\mu_{\text{MLDL}} = \left(\frac{1 - x_1}{\mu_{\text{amphibole}}} + \frac{x_1}{\mu_{\text{MARID}}} \right)^{-1} \quad (11)$$

With a weaker MLDL rheology, delamination happens faster and finishes within ~ 3 Ma (see Figure 9). In both experiments, the strength of the MARID layer (10 km thick, with an $\sim 10^{18.5}$ viscosity) is the factor controlling the speed of keel tearing during the delamination event is, not the viscosity of the surrounding mantle. This behavior is consistent with the analytical model. The implied duration for a 1,000-km-wide regional keel delamination event would be shorter than 10 Myr. These implied tearing rates (>100 km/Myr) are faster than the magmatism-indicated keel removal rates for the ENCC (~ 17 Myr for $\sim 1,000$ km) or the WWC (~ 11 Myr for ~ 400 km; see Figure 1). Assuming the thickness of the MLDL layer is appropriate, then the MLDL should have a composition with a rheology stronger than that of a pure MARID component.

5.2.2. Delamination Along a MLDL Due to Chemically Bound Water

A MLDL has also been interpreted as a water-rich intracratonic layer (origin 1 in the section 1), with a rheology dominated by wet olivine. At 80–100-km depths within a 200-km craton (i.e., ~ 700 – 800 °C, ~ 3 GPa), the chemically bound water content has been proposed to be $>1,000$ ppm (Karato et al., 2015). If the MLDL contains 60% olivine, 12% clinopyroxene, and 28% orthopyroxene (cf. Hirschmann et al., 2009), the water content in olivine is estimated >214 ppm (see water partition coefficients in the Table 1). With 1.93 exponent factor (Korenaga & Karato, 2008) for the effect of water on diffusion creep, the MLDL is predicted to be >11 times weaker than a wet olivine (61 ppm) rheology.

In run 4, the MLDL is assumed to have a wet (214 ppm) olivine rheology. In this case, lower keel delamination starts ~ 11 Myr after the onset of the experiment (see Figure 9). A 1,000-km-wide regional keel delamination event ends at ~ 36 Myr, the delamination process taking ~ 25 Myr. This predicted delamination rate (~ 40 km/Myr) is consistent with evolution on the WWC but somewhat slower than that (~ 60 km/Myr) of the ENCC (see Figure 1).

5.2.3. Keel Delamination Along a MLDL With a Rheology Shaped by Both Metasomatism and Chemically Bound Water

Geochemical observations on the ENCC can be interpreted to hint that both MARID-like metasomatic components and water-rich peridotites coexisted within the MLDL before the ENCC keel's destruction (Menzies et al., 1993; Xia et al., 2013; Xu, 2001; Xu et al., 2009; Zhu et al., 2012). What if some MLDLs are rheologically weak because of both effects, for example, they consist of a wet peridotite layer that contains discrete interbedded MARID lamellae, with a composite rheology governed by an analog to equation (11)?

In runs 5 and 6, we assumed that the MLDL is composed of (a) 10% (volume percentage) MARID + 90% wet peridotite or (b) 20% MARID + 80% wet peridotite. In both runs, the MLDL's effective viscosity (μ_{MLDL}) is calculated assuming the bulk rheology given in equation (11), where x_1 is the volume proportion of the first component. Because the MLDL in run 5 contains a lower proportion (10%) of the MARID component, its effective viscosity is higher. In this case, the keel delamination takes ~ 18.3 Myr, ~ 1.3 Myr longer than that of the run 6 (see Figure 9). In run 6, the keel delamination starts at ~ 8 Myr after the onset of the far-field subduction, and 1,000-km-wide regional keel delamination takes ~ 17.1 Myr. Both of these appear to be consistent with geological observations for the ENCC.

5.3. Other Factors Affecting Keel Delamination

5.3.1. Effects of MLDL Melting

If the MLDL is mainly due to chemically bound water (Karato et al., 2015), the high-water content will also lower the solidus of the layer (see equation (A15); cf. Katz et al., 2003). During partial melting, water in peridotite is thought to partition into melt roughly like Ce, with a ~ 0.009 peridotite/melt partition coefficient (Aubaud et al., 2004). In this case, the dehydration effect of potential melting process will tend to harden the residual MLDL. We have studied possible effects of MLDL melting on keel delamination with run 7. This run is similar to the conditions in run 6, except that it includes the effect of water (1,000 ppm) on MLDL melting.

In this run (Figure 10), MLDL melting happens near the beginning of the experiment and is focused within a small and relatively hot region close to the craton's margin. During subsequent keel tearing and delamination

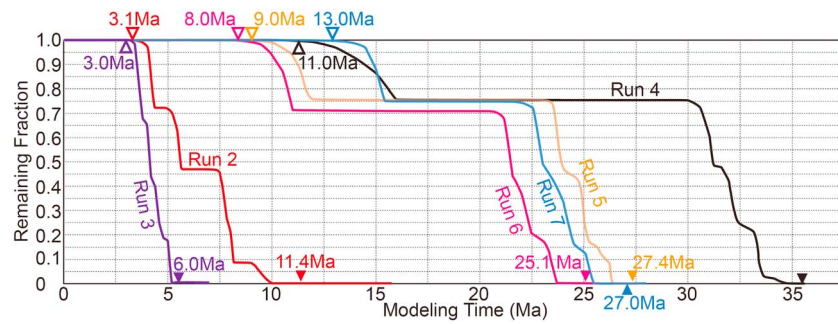


Figure 9. The progress of keel tearing and delamination during runs 2–7. The remaining fraction of the lower keel is calculated by L_R/L_I , where L_I is the initial horizontal keel extent (1,000 km) beneath the midlithospheric discontinuity layer, and L_R is the remaining horizontal keel extent beneath the midlithospheric discontinuity layer.

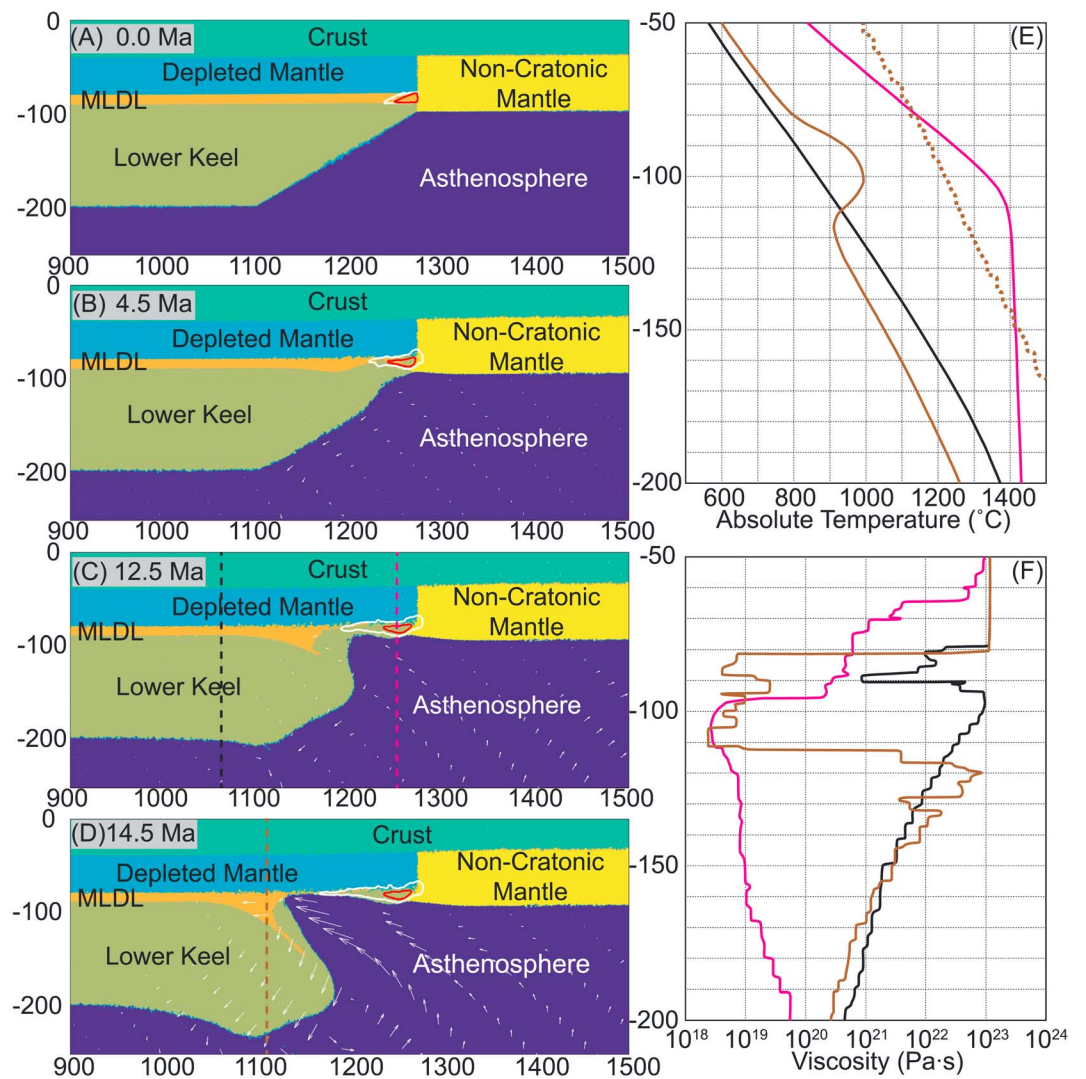


Figure 10. Melting effects on keel delamination. (a)–(d) show results from run 7. White contours mark regions where melting happens (with melting degree $f > 0$); red contours mark regions with melting degree $> 2\%$. Short white lines with arrow mark the direction of local convection. (e) Temperature profiles along the corresponding vertical-dashed lines of the same color in (c) and (d). The mantle solidus (brown dashed line) is plotted along the dashed line in (d) (see method in Appendix A). Note that: the MLDL remains its low temperature and does not melt during the delamination of the lower keel. (f) Viscosity profiles along the corresponding vertical dashed lines of the same color in (c) and (d). MLDL = midlithospheric discontinuity layer.

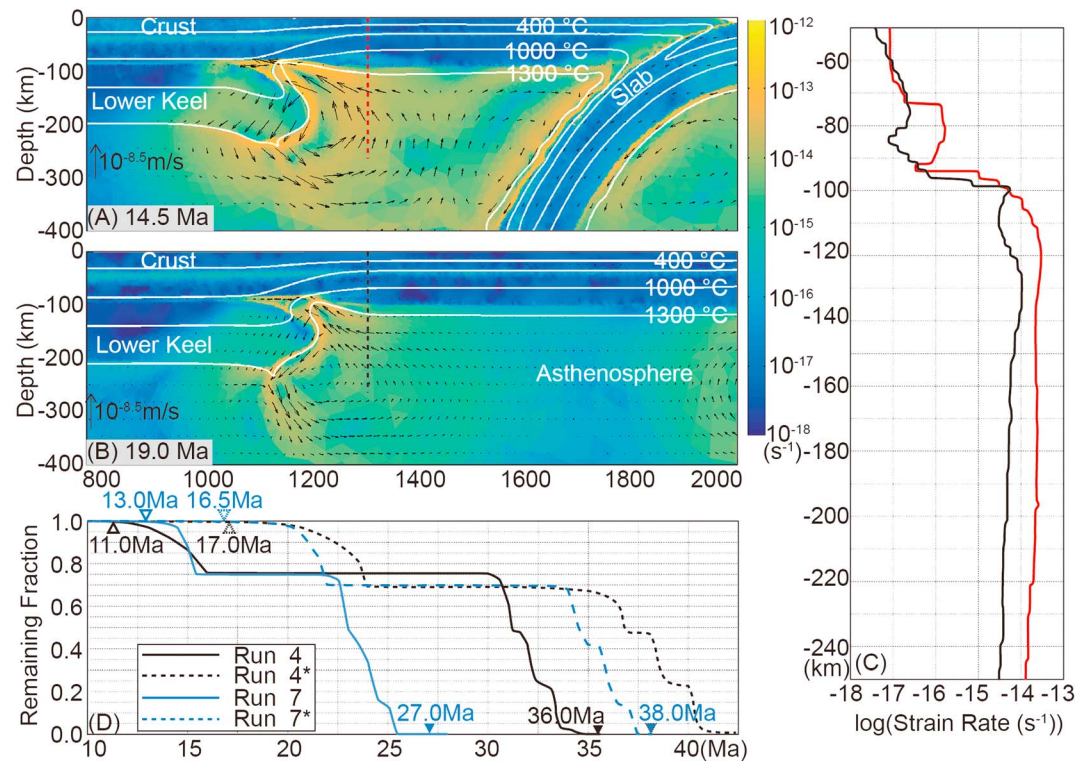


Figure 11. Effects of far-field subduction on keel delamination. (a) and (b) are plots of second invariant of strain rate during runs 7 and 7*. (c) The second invariant of strain rate along the corresponding vertical-dashed lines of the same color in (a) and (b). (d) The keel tearing and delamination progress during runs 4, 7 (with subduction) and runs 4*, 7* (without subduction). Plot conventions are the same as in Fig. 9.

(Figures 10b–10d), the melting region does not expand. This happens because flow within the MLDL is horizontal flow of cool MLDL material (see Figure 10e). Limited melting can dehydrate a small fraction of the MLDL, thereby transforming it into a drier and stronger residue (see Figures 10b–10d). This process is equivalent to supplying a mechanically different component at the end of the conduit (see Figure 4). Since the dehydrated material is stronger, the keel’s tearing rate slows. In this run, keel delamination starts at ~13 Ma, ~ 8 Ma later than that of run 6 (see Figure 9). However, because pervasive melting of MLDL does not happen during keel delamination, the evolution in this run is quite similar to run 6 (see Figure 9). This is also the reason that we do not view MLDL melting as a major factor when delamination happens. The paper 2 studies the melting processes that follow keel delamination.

5.3.2. Effects of Far-Field Subduction

Because the ENCC and the WWC keel-removal events may be related to subduction-craton interactions (cf. English & Johnston, 2004; Snyder et al., 1976; Zhu et al., 2012), we have also explored experiments that study the potential effects of subduction on the tearing mode of keel delamination.

The far-field subduction condition is removed in runs 4* and 7*, which are otherwise similar to runs 4 and 7. Without nearby regional subduction (see Figure 11), the onset of keel delamination is slower. This occurs because far-field subduction induces more vigorous flow in the asthenosphere near the keel’s edge that weakens its power-law-creep-dependent viscosity (see Figures 11a and 11b). We see that strain rates in runs 4 and 7 are generally higher than those of runs 4* and 7* (see Figure 11c), so that mantle material close to the MLDL in runs 4 and 7 is weaker than that in runs 4* and 7*. This weaker surrounding mantle can more easily flow into the MLDL to fill the void left by keel tearing and delamination (see Figure 5c).

6. What Controls the Depth of the MLDL?

As noted above, the cause of the MLDL remains uncertain. Long-lived mantle metasomatism has been proposed to be the cause of the MARID layer observed in kimberlite xenoliths. The usual

thermodynamic rationale for its location at ~80–100-km depths is that these are the p-T conditions at which MARID minerals exsolve and form in reactions between mantle and ascending volatile-rich CO₂-rich hydrous magmas (Eggler, 1978; Dalton & Presnall, 1998). The melts that periodically infiltrate the lithosphere would be created by deeper upwellings at the craton base that generate fluid-rich hydrous magmas (kimberlites in crude sense; cf. Choukroun et al., 2005; O'Reilly & Griffin, 2013). Episodic reheating of the base of a craton could induce partial melting associated with repeated upward migrations of these magmas to MLDL depths of reaction/exsolution (see also Griffin et al., 2014; Malkovets et al., 2007). Sleep (personal communication, March 20, 2018) has suggested the alternative mechanism that there may be a rheological control that leads to preferential ponding of CO₂-rich hydrous magmas at the MLDL depth that they pond at the base of the lithosphere's brittle-ductile transition in its strength *Christmas tree* (Sleep, 2009). Finally, lithospheric *stacking* during subduction has also been proposed as the origin for a craton and its MLDL, with the MLD reflecting the interval between the two lithospheric slices (Lee et al., 2011).

Once formed within a craton, a MLDL can stably remain until the craton's edge is destroyed. For example, episodic and rapid back-arc extension during the evolution of subduction (cf. Faccenna et al., 2001) could induce lithospheric extension close to the edge of the craton's MLDL (e.g., at ca. 180 Ma; Maruyama et al., 1997) and so create a geometry like the initial geometry assumed in Figure 6.

7. Similarities and Differences Between Analytical and Numerical Results

In many respects, the numerical experiments replicate basic aspects of the analytical lubrication-theory-based solutions. Keel delamination does not occur over an Archaean craton's lifetime when a tens of kilometers wide region at the edge of the MLDL has viscosities of order 10²³ Pa·s. Geologically, rapid delamination happens when a MLDL is *exposed* to nearby low-viscosity (<10²¹ Pa·s) asthenosphere. Other behavior is different. In numerical experiments, the delaminating keel breaks into ~200–300-km-wide fragments as delamination progresses. While geologically rapid, the delamination process itself occurs in jerks, with pulses of rapid delamination ending as a keel fragment breaks away. This jerkiness in delamination is linked to lateral flow within the MLDL, with lateral flow allowing the MLDL to preferentially thicken in regions undergoing slow delamination (see Figure 12b) while also increasing lateral pressure gradients in regions adjacent to the delamination front. Tearing jerks are also linked to fragmentary keel breakoff, with breakoff associated with simultaneous local uplift (Figure 12) and a reduction in the net negative buoyancy of the keel—the driving force for delamination.

7.1. Postdelamination Uplift

The 2-D numerical experiments indicate potential postdelamination uplift, which not apparent in 1-D experiments. After keel delamination, the surface expression is ~600–900-m uplift (see Figure 12 and supporting information Movies S4), significantly less than the uplift of order ~3 km predicated in previous studies (Krystopowicz & Currie, 2013). (Total uplift will be related to the net density contrast between removed keel and infilled asthenosphere.) This suggests that delamination may not be associated with the creation of a *high plateau* that reverses the source direction of local sediment transport. Therefore, the scenario here does not appear to contradict sedimentary records which suggest that during the Mesozoic (ca. 180–150 Ma) portions of the North China remained relatively low in elevation and still accepted sediments from its surrounding continental blocks (H.-Y. Li et al., 2013). Delamination is also likely to be associated with postdelamination extension that can create local depocenters.

8. Implications for Global Rates of Craton Destruction

Even with generous estimates for keel destruction beneath the ENCC and WWC, the implied recent rate of craton destruction is relatively small. For the ENCC, the surface area above the destroyed keel is estimated to be 5.7×10^5 km² (D. He et al., 2015). For the WWC, the most conservative estimate for the surface area above the destroyed keel is the area to the west of 110-km-thickness contour on the WCC (Figure 1b), which is $\sim 3.8 \times 10^4$ km² (38% of the total area; Chamberlain et al., 2003). If these two keel fragments were the only sites of keel delamination within the past 200 Myr, the implied destruction rate would be 6.1×10^5 km²/200 Ma = 3.1×10^6 km²/Gyr. The remaining cratonic fraction of continents is estimated to have a surface

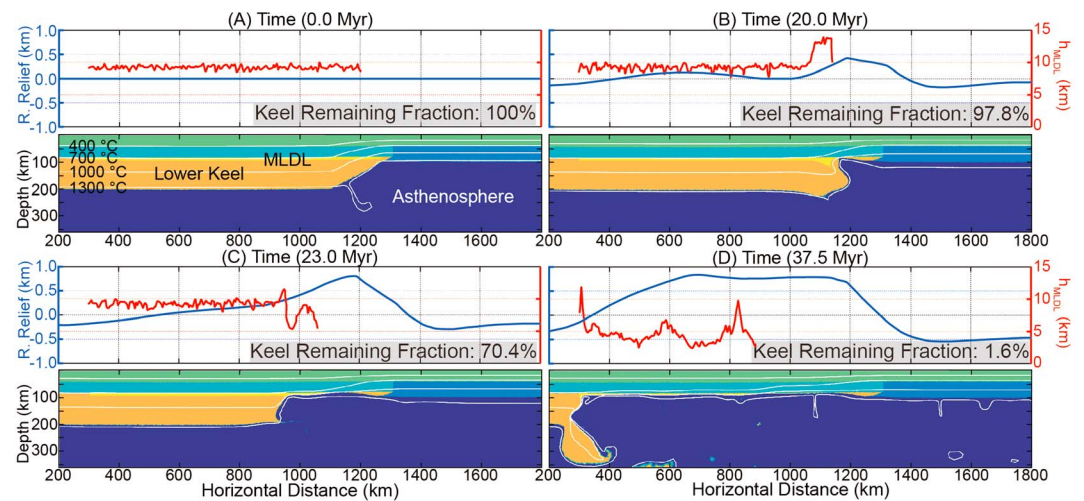


Figure 12. The evolution of surface relief and MLDL thickness. Four snapshots of relative relief, MLDL thickness, and material phase are plotted for run 7* (see Table 2 and Figure 9). Relative relief (R. Relief) is calculated by subtracting the surface relief from the first time step (a). Because the effects of erosion and sedimentation are not considered in the numerical experiments, relative relief can only crudely delimit delamination-induced variations in relief. See the Movies S1–S10 for more insight into these time-dependent phenomena. MLDL = midlithospheric discontinuity layer.

area of $3.7 \times 10^7 \text{ km}^2$ (Artemieva, 2012), which would imply that modern rates of craton destruction would destroy 14% of the original craton area over 2 Gyr or 25% of the original craton area over 4 Gyr. Even assuming that paleo-destruction rates were likely to be faster during the Archean, modern rates of keel destruction are consistent with continents still retaining a large surviving craton area.

9. Lateral Variability in Cratonic Keel Removal

Although regional cratonic keel removal has been reported in the ENCC, the WWC, and possibly beneath parts of the Dharwar and the Brazilian Cratons, neighboring parts of these cratons still maintain their apparently stable thick cratonic state. This suggests that keel delamination is both rare and piecemeal. In our preferred scenario, this happens because

1. MLDLs are laterally discontinuous and variable (see Figure 2b; Chen et al., 2014; Hopper et al., 2014). In this case, cratonic parts without well-developed MLDLs survive due to their internal integrity (see Figure 8d). Discontinuous MLDLs can be created by spatial and/or temporal variations during their formation. For example, intracratonic compositional layering in the Kalahari Craton may be linked to multiple kimberlite intrusion episodes in different epochs (O'Reilly & Griffin, 2013). MLDL continuity can also be disturbed by episodic reheating and MLDL melting near cratonic edges, or where internal intracratonic boundaries are reheated by mantle plume-related processes (Griffin et al., 2014). Sharp vertical changes in adjacent MLDL depths could be created by strongly varying lateral temperature conditions at the time of metasomatism of each section of the discontinuous MLDL, for example, due to the existence of thicker crust beneath ancient block boundaries (Kinck et al., 1993; Youssof et al., 2013). This too would tend to increase the resistance of the craton to pervasive keel delamination.
2. The cratonic keel's fertility and compositional density may also be laterally inhomogeneous, which can be directly linked with heterogeneity in the MLDL (i.e., if both are due to metasomatic processes; Artemieva & Vinnik, 2016; Griffin et al., 2003; Kaban et al., 2003, 2016; Mooney & Kaban, 2010). Less fertile and more compositionally buoyant keel regions may better resist delamination (see Figure 5). A more fertile keel state should naturally tend to appear at a craton's margin, due to the enhanced tendency for plume and/or asthenosphere melting beneath the thinner keel edges. The spatial scales for keel refertilization events can be limited, for example, if some plume-related events have led to the keel refertilization in southwestern Kalahari Craton (Griffin et al., 2003), keel refertilization may have been limited to the sizes of the plume tails (~100 km in diameter) or the lateral extent of drainage associated with lateral plume flow (Yamamoto et al., 2007).

10. Conclusions

1. We propose an intracratonic keel delamination model inspired by observations of geologically recent delamination events beneath the ENCC and WWC. This scenario is summarized in Figure 3. The weak intralithospheric MLDL at ~80–100-km depths is the preferred site for keel tearing and delamination from overlying crust and lithosphere. Keel tearing can occur in situations when lateral flow within the MLDL *tear* can connect to inflow from nearby weak asthenosphere. Delamination can be slightly sped up by ongoing far-field subduction or any mechanism that reduces the viscosity of the mantle at the craton's edge.
2. Keel delamination along a water-rich or MARID-bearing MLDL can explain the geologically implied keel removal speeds observed on the WWC in North America and the ENC in China. However, if the craton's surrounding lithosphere stays thick, for example, >140 km, and therefore relatively strong (e.g., >10²³ Pa·s), a fertile and negatively buoyant cratonic keel overlain by a weak MLDL will remain stable over billions of years.
3. Cratonic keel delamination appears to be independent of the weak intracratonic layer's density; delamination still occurs when the MLDL's net density is lower than that of keel and asthenosphere. Lateral variations in the distribution of the MLDL and/or in the fertility of its underlying keel are more important factors to lead to cratonic keel destruction.

Appendix A: Details of the Numerical Implementation for Thermomechanical Deformation and Melting

This appendix describes the algorithms that are used in this study. A modified version of 2-D Lagrangian finite element code, “m2tri_trunk” (Hasenclever, 2010) based on the approaches used in “MILAMIN” (Dabrowski et al., 2008), is used. This thermomechanical code solves for heat transport and elastoviscoplastic deformation in crust and mantle rocks. The supplement shows a benchmark of this code against a recent subduction benchmark study (Schmeling et al., 2008; see supporting information S1).

A1. Temperature

For computational simplicity, temperature is treated as a potential temperature. The thermal calculation includes the effects of thermal diffusion, thermal convection, radioactive heating, and shear heating (viscous dissipation; equation (A1)).

Temperature is determined from an equation governing energy conservation:

$$\rho C_p \frac{\partial T}{\partial t} = \frac{\partial}{\partial x} \left(K \frac{\partial T}{\partial x} \right) + \frac{\partial}{\partial z} \left(K \frac{\partial T}{\partial z} \right) + H, \quad (\text{A1})$$

where ρ is density, C_p is heat capacity, t is time, K is thermal conductivity, and H is the volumetric heat production rate (including both radioactive heating and viscous dissipation).

A2. Elastoviscoplastic Deformation

The different materials used in the model are treated as incompressible materials with use of the Boussinesq approximation (Turcotte & Schubert, 2014). Tracer particles are used to track seven different compositional materials (e.g., upper crust and asthenosphere). See Figure 6 for the definitions of each possible material type. Each material type is associated with a specific rheology that is potentially ρ , T , strain rate, accumulated strain, and plastic yield-stress dependent. Table 1 gives the values assumed for the experiment. The number of tracer particles within each element ranges between 7 and 25. Viscosity is calculated at every integration point using the material phase determined by the nearest tracer particle within the element. Density is also uniform within each element with a value determined by the average of the density of each of the tracer particles within the element.

For each tracer particle, density is temperature and pressure dependent (equations (A7) and (A8); Djomani et al., 2001; Schutt & Leshner, 2006). Each material rheology can include elastic, viscous, and plastic effects. Yielding and plastic flow behavior are calculated using the method described in Moresi et al. (2003).

Elastoviscoplastic deformation is described using the equations for force equilibrium ((A2) and (A3)) and mass conservation (A4):

$$\frac{\partial}{\partial x} \left(\eta_{VEP} \left(\frac{4}{3} \frac{\partial u}{\partial x} - \frac{2}{3} \frac{\partial v}{\partial z} \right) \right) + \frac{\partial}{\partial z} \left(\eta_{VEP} \left(\frac{\partial u}{\partial x} + \frac{\partial v}{\partial z} \right) \right) - \frac{\partial P}{\partial x} = f_x + F_x^{e,t} \quad (A2)$$

$$\frac{\partial}{\partial z} \left(\eta_{VEP} \left(\frac{4}{3} \frac{\partial v}{\partial z} - \frac{2}{3} \frac{\partial u}{\partial x} \right) \right) + \frac{\partial}{\partial x} \left(\eta_{VEP} \left(\frac{\partial u}{\partial x} + \frac{\partial v}{\partial z} \right) \right) - \frac{\partial P}{\partial y} = \rho g + f_y + F_y^{e,t} \quad (A3)$$

$$\frac{\partial u}{\partial x} + \frac{\partial v}{\partial z} = -\frac{P}{\kappa} \quad (A4)$$

In these equations, u and v refer to horizontal and vertical velocity components, respectively, P is the dynamic pressure, g is the acceleration of gravity, and κ is the penalty term used for ensuring incompressibility with κ being 10^6 times the maximum effective viscosity (η_{VEP} ; Hasenclever, 2010). $F_i^{e,t}$ is the internal elastic stress (Moresi et al., 2003) that can be advected by material flow. This behavior is described as

$$F_i^{e,t} = -(\eta_{VEP}/G\Delta t)(\partial \tau_{ij}^{old} J / \partial x_i + \partial \tau_{ii}^{old} J / \partial x_j), \quad (A5)$$

where G is elastic shear modulus, Δt is time step, and $\tau_{ij}^{old} J$ is the Jaumann-rotated stress of the previous time (Kaus et al., 2010), given by

$$\tau_{ij}^{old} J = \tau_{ij}^{old} - \omega_{ik}^{old} \tau_{ki}^{old} + \tau_{ik}^{old} \omega_{ki}^{old}, \quad (A6)$$

where τ_{ij}^{old} is the deviatoric stress from the previous time step, and $\omega_{ij} = 1/2(\partial u_i / \partial x_j - \partial u_j / \partial x_i)$.

The equation of state for density is

$$\rho = \rho_0 \exp \left[-\int_{T_0}^{T_F} \alpha(P = P_0, T) dT + \int_{P_0}^{P_F} \frac{dP}{k} \right], \quad (A7)$$

$$\alpha = \alpha_0 + \alpha_1 T + \alpha_2 T^{-2}, \quad (A8)$$

where ρ_0 is the reference density, α is the temperature dependent thermal expansion coefficient at $T_0 = 20^\circ\text{C}$, P_0 is atmospheric pressure, k is the bulk modulus (assumed to be constant), and T_F and P_F are the temperature (in Kelvin) and pressure, respectively.

A temperature-dependent accumulated strain weakening effect is also included. This effect appears when large strains accumulate within a rock, inducing crystal lattice reorientation and recrystallization. Lattice reorientation can reduce the viscosity in dislocation creep (Tommasi et al., 2009) as weaker slip systems become the preferred slip systems. Recrystallization can lead to a reduction in crystal grain size. In turn, the mean grain size d is thought to affect viscosity during diffusion creep by its dominant effect on grain boundary diffusion (Hirth & Kohlstedt, 1995). This yields a power law dependence of approximately -3 (Dimanov et al., 2003; Hirth & Kohlstedt, 2004; Xiao et al., 2002), for example, the preexponent A is given by

$$A(d) = A_0 d^{-3}, \quad (A9)$$

where A_0 is a constant, and d is grain size.

These combined effects are commonly called *strain weakening*.

Strain weakening is temperature dependent since temperature shapes the *equilibrium* grain size in a dynamically recrystallizing system. At “high-enough” temperatures, crystals can more rapidly grow/recover to reach their preferred state of dynamic equilibrium. In this case, the preferred crystal size is relatively large, and strain weakening effects for diffusion creep are less significant. At “lower” temperatures, Arrhenius-law-governed crystal growth rates are much slower. The resulting reduced grain-size in *dynamic equilibrium* can lead to pronounced strain weakening during diffusion creep. The threshold temperature where this effect becomes significant is approximately 800°C (Précigout et al., 2007) for natural subcontinental peridotites.

Table A1
Parameters for Temperature-Dependent Strain Weakening Recovery

	Mantle	Crust
T_{lower}	1,073.15 K	473.15 K
T_{upper}	1,573.15 K	973.15 K
$A_{\text{diffusion}}$	-14.4892	-7.6140
$A_{\text{dislocation}}$	-7.2446	-3.1324
$S_{\text{max dislocation}}$	10	5
$S_{\text{max diffusion}}$	100	50

We parameterize temperature-dependent accumulated strain weakening as a function of the second invariant of finite strain and the material-dependent temperature where viscous creep dominates plastic yielding effects (see equations (A10)–(A12)). Different maximum accumulated strain weakening coefficients are used for diffusion creep and dislocation creep (see Table A1).

$$S = S_{\text{max}} \cdot \min(1, \gamma/\gamma_0), \quad T < T_{\text{lower}}, \quad (\text{A10})$$

$$S = S_{\text{max}} \cdot \exp\left(A \frac{T - T_{\text{upper}}}{T_{\text{upper}}}\right) \cdot \min(1, \gamma/\gamma_0), \quad T_{\text{lower}} \leq T \leq T_{\text{upper}}, \quad (\text{A11})$$

$$S = 1, \quad T > T_{\text{upper}}. \quad (\text{A12})$$

In equations (A10)–(A12), S is the weakening factor, γ is the second invariant of finite strain (E_{KL} , see equation (A13)), $\gamma_0 = 1.5$ is the critical value for γ , A is given in Table A1, and T_{lower} and T_{upper} are the lower and upper temperatures of the temperature range where accumulated strain weakening can relax due to a larger grain size at dynamic equilibrium, respectively. Finite strain is calculated using the form of Green-Lagrangian strain tensor (see equation (A13); cf. the method discussed in Chapter 4 of Malvern, 1969).

$$E_{KL} = \frac{1}{2} \left(\frac{\partial x_i}{\partial X_K} \frac{\partial x_j}{\partial X_L} - \delta_{KL} \right), \quad (\text{A13})$$

where E_{KL} is the finite strain tensor, δ_{KL} is the Kronecker delta. The displacement gradient $\frac{\partial x_i}{\partial X_K}$ is described as

$$\frac{\partial x_i}{\partial X_K} = \frac{\partial x_i}{\partial X_{K\text{old}}} + dt \left(\frac{\partial \mu_i}{\partial x_i} \frac{\partial x_i}{\partial X_{K\text{old}}} + \frac{\partial \mu_j}{\partial x_j} \frac{\partial x_j}{\partial X_{K\text{old}}} \right), \quad (\text{A14})$$

where u_i is velocity vector, and $\frac{\partial x_i}{\partial X_{K\text{old}}}$ is the displacement gradient of the previous time step.

A3. Melting

Material melting is found using methods described in Hasenclever (2010) and Morgan (2001) with the mantle solidus T_m given by equation (A15) (see Figure A1). We have also considered the effects of melting degree f and water content $X_{\text{H}_2\text{O}}$ on the solidus (Katz et al., 2003; Morgan, 2001). For each time step, the melting process is modeled using the following recipe that is an extension of the approach developed in Morgan (2001):

1. Heat-induced melting. If the temperature T_a (transformed from the potential temperature T with a 0.33 K/km adiabatic gradient) lies above the solidus $dT = T_a - T_m > 0$, then a heat-induced melting degree increment df_{heat} will occur. The amount is calculated with equation (A16). The temperature after melting is set to the solidus determined from the updated degree of melting and water content.
2. Pressure release melting. If upwelling leads to a pressure decrease dP , and the material is at its solidus, melting will also occur. In this case, the degree of melting and new solidus is updated according to the new pressure (Morgan, 2001). The pressure-release-induced melting degree increment df is calculated using equation (A17) (see equation 11 in Morgan, 2001). The temperature of the melting parcel is then updated to the new depletion-dependent solidus. For increased stability, the melting increment is calculated iteratively, if $df_{\text{heat}} > df$ (e.g., $\delta f = 0.01$) in the first or $dP > \delta P$ (e.g., $\delta P = 0.001$ GPa) in the second.

$$T_m = T_0^m + \left(\frac{\partial T^m}{\partial P} \right)_f P + \left(\frac{\partial T^m}{\partial f} \right)_P f - 43 \cdot X_{\text{H}_2\text{O}}^{0.75}, \quad (\text{A15})$$

$$\left(\frac{df}{dT} \right)_{\text{heat}} = 1 / \left(\left(\frac{\partial T^m}{\partial f} \right)_P + \frac{Q_L}{C_p} \right), \quad (\text{A16})$$

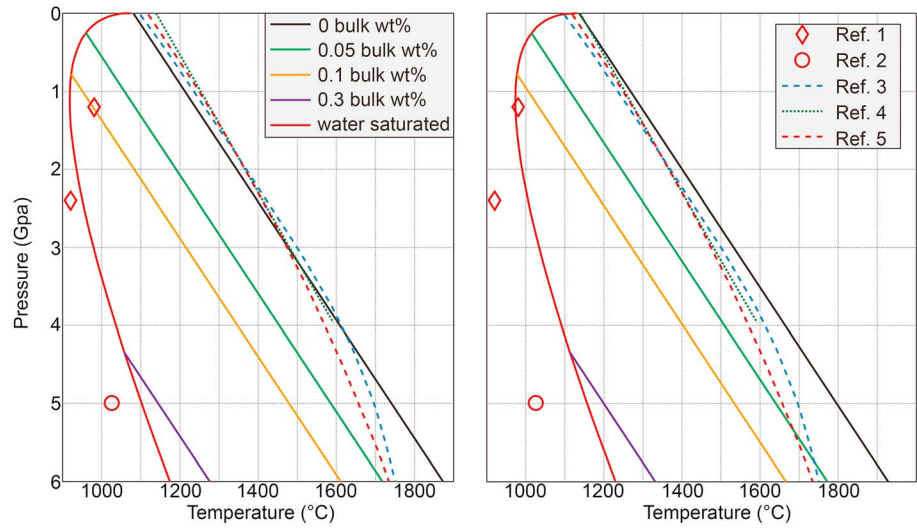


Figure A1. The solidus for different bulk water contents of asthenosphere/midlithospheric discontinuity layer material (left) and lithospheric mantle (right). Following Katz et al. (2003), the dissolved water's effect on solidus is taken to be linear and bounded by the saturation of water in the melt. "0.05 bulk wt. %, etc." are labels for the water content used to determine the corresponding solidus.

$$-\left(\frac{df}{dP}\right)_s = \left(\left(\frac{\partial T^m}{\partial P} \right)_f - \frac{\alpha T}{\rho c_p} \right) / \left(\frac{Q_L}{c_p} + \left(\frac{\partial T^m}{\partial f} \right)_p \right), \quad (\text{A17})$$

where T_0^m is the solidus at room temperature and pressure, α is thermal expansion coefficient, Q_L is latent heat during melting, $(\partial T^m / \partial f)_p$ describes the solidus's dependence on degree of melting, and $(\partial T^m / \partial P)_f$ describes the solidus's dependence on pressure. Table 1 shows the parameters used in the numerical experiments.

Appendix B: Meshing and Remeshing

The computational domain is a mesh of triangular elements that is built using an adaptive mesh generation algorithm that makes element sizes be relatively small (~ 4.5 km) when near internal boundaries between different materials (see equations (B2)–(B4)). Element sizes are made to be 10 times larger than this (~ 40 km) in regions far from internal material interfaces, while at transitional distances, element size is linearly interpolated between these two end-member values. This approach guarantees relatively high resolution along material interfaces and within thin material layers during a calculation. We find that material interfaces remain well tracked even when high velocities occur due to the effects of slab subduction and keel tearing and sinking (see Figures 8 and S3). Because we use a Lagrangian approach in which straight-sided element vertices advect with material flow, some elements can become heavily distorted in regions of strong shear. A new equant-element mesh is regenerated by remeshing whenever elements are deemed to be *too distorted* (this is defined to be when any interior angle of an element is larger than 170° or smaller than 7° , or any mesh quality factor Q is smaller than 0.2, see equation (B1)). In run 1, the Lagrangian approach is only used for the portion with temperature $> 1,150$ $^\circ\text{C}$; a semi-Lagrangian approach (Hasenclever, 2010) is used for the remaining deeper portion (the more ductile asthenosphere) in order to minimize computational time. Equations (B2)–(B4) are used to define the preferred element size R as a function of distance r from an internal boundary interface.

$$Q = (L_2 + L_3 - L_1)(L_1 + L_3 - L_2)(L_1 + L_2 - L_3) / (L_1 L_2 L_3), \quad (\text{B1})$$

where L_1 , L_2 , and L_3 are the side lengths of the triangular element.

$$L_0 = R_2 \text{ when } r > 4.75 \cdot R_2, \quad (\text{B2})$$

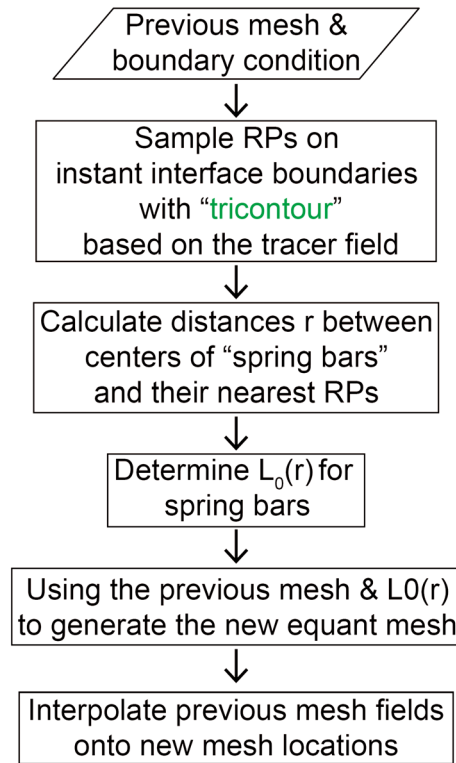


Figure B1. Flowchart for the adaptive mesh resizing algorithm. Reference points (RPs) are the points used to determine the characteristic element size as a function of spatial position (e.g., distance from nearest RP). The characteristic element size L_0 (or the characteristic bar length for *virtual spring* connecting element vertexes; Persson & Strang, 2004) is determined based on equations (B2)–(B4). “Tricontour” is an open source MATLAB function developed by Darren Engwirda, (see <https://uk.mathworks.com/matlabcentral/fileexchange/10408-contours-for-triangular-grids?focused=5068781&tab=function>). It is used to resample RPs on the contoured interfaces between different materials within the unstructured triangular mesh. The sampling distance for RPs is determined by the number of tracer particles in nearby elements, which ranges from 7–25 per element.

$$L_0 = \frac{r}{3.75 \cdot R_2} (R_2 - R_1) + R_1 \text{ when } R_1 < r \leq 4.75 \cdot R_2, \quad (\text{B3})$$

$$L_0 = R_1 \text{ when } r \leq R_1, \quad (\text{B4})$$

Acknowledgments

This work was supported by the Chinese Academy of Sciences (Grant No. XDB18000000), the State Oceanography Bureau (Grant No. GASI-GEOGE-02) and the National Natural Science Foundation of China (Grant No. 41688103). We thank the Guangzhou Institute of Geochemistry, Chinese Academy of Sciences and Royal Holloway, University of London for supporting this PhD work. We thank the associate editor, anonymous reviewer, and Norm Sleep for helpful suggestions to restructure and improve the submitted manuscript. We also thank Norm Sleep for his suggestions on the potential formation mechanism for the metasome/MLDL. There are no data sharing issues since all of the numerical information is provided in the figures and movies produced by solving the questions in the appendixes with initial and boundary conditions and parameters given in the paper.

where L_0 is the characteristic element size used for a certain set of coordinates, r is distance between center of *spring bar* connecting element vertexes (Persson & Strang, 2004) to its closest reference point (RP) sampled along an interphase boundary. R_1 is the smallest element size (here 4.45 km), and R_2 is the largest size (44.32 km). The adaptive algorithm to determine the preferred element sizes over the computational domain is shown in Figure B1. It first samples RPs on the interfaces between different material types using the MATLAB function “tricontour.” It then determines how far the center of each spring bar is from its nearest RP and assigns a preferred length size R to the center of each spring bar. This mesh-size information is used to generate a new relatively equant mesh of triangles using a finite-element-reformulated version of the DISTMESH algorithm (Persson & Strang, 2004) done by Taramón et al. (2017). The last step is to interpolate the current variable fields onto the new mesh.

References

- Abt, D. L., Fischer, K. M., French, S. W., Ford, H. A., Yuan, H. Y., & Romanowicz, B. (2010). North American lithospheric discontinuity structure imaged by Ps and Sp receiver functions. *Journal of Geophysical Research*, *115*, B09301. <https://doi.org/10.1029/2009JB006914>
- Andrés-Martínez, M., Morgan, J. P., Pérez-Gussinyé, M., & Rüpke, L. (2015). A new free-surface stabilization algorithm for geodynamical modelling: Theory and numerical tests. *Physics of the Earth and Planetary Interiors*, *246*, 41–51. <https://doi.org/10.1016/j.pepi.2015.07.003>

- Artemieva, I. M. (2012). A lithospheric perspective on structure and evolution of Precambrian cratons. In D. Roberts & A. Bally (Eds.), *Regional geology and tectonics: Principles of geologic analysis* (pp. 94–111). Amsterdam: Elsevier.
- Artemieva, I. M., & Vinnik, L. P. (2016). Density structure of the cratonic mantle in southern Africa: 1. Implications for dynamic topography. *Gondwana Research*, 39, 204–216. <https://doi.org/10.1016/j.gr.2016.03.002>
- Aubaud, C., Hauri, E. H., & Hirschmann, M. M. (2004). Hydrogen partition coefficients between nominally anhydrous minerals and basaltic melts. *Geophysical Research Letters*, 31, L20611. <https://doi.org/10.1029/2004GL021341>
- Aulbach, S., Massuyeau, M., & Gaillard, F. (2017). Origins of cratonic mantle discontinuities: A view from petrology, geochemistry and thermodynamic models. *Lithos*, 268, 364–382.
- Bao, X., Eaton, D. W., & Guest, B. (2014). Plateau uplift in western Canada caused by lithospheric delamination along a craton edge. *Nature Geoscience*, 7(11), 830–833. <https://doi.org/10.1038/ngeo2270>
- Batchelor, G. K. (2000). *An introduction to fluid dynamics* (p. 615). Cambridge, UK: Cambridge University Press.
- Begg, G., Griffin, W., Natapov, L., O'Reilly, S. Y., Grand, S., O'Neill, C., et al. (2009). The lithospheric architecture of Africa: Seismic tomography, mantle petrology, and tectonic evolution. *Geosphere*, 5(1), 23–50. <https://doi.org/10.1130/GES00179.1>
- Bird, P. (1979). Continental delamination and the Colorado Plateau. *Journal of Geophysical Research*, 84(Nb13), 7561–7571.
- Brune, S., Heine, C., Perez-Gussinye, M., & Sobolev, S. V. (2014). Rift migration explains continental margin asymmetry and crustal hyperextension. *Nature Communications*, 5(1), 4014. <https://doi.org/10.1038/ncomms5014>
- Chamberlain, K. R., Frost, C. D., & Frost, B. R. (2003). Early Archean to Mesoproterozoic evolution of the Wyoming Province: Archean origins to modern lithospheric architecture. *Canadian Journal of Earth Sciences*, 40(10), 1357–1374. <https://doi.org/10.1139/e03-054>
- Chen, L., Jiang, M. M., Yang, J. H., Wei, Z. G., Liu, C. Z., & Ling, Y. (2014). Presence of an intralithospheric discontinuity in the central and western North China Craton: Implications for destruction of the craton. *Geology*, 42(3), 223–226. <https://doi.org/10.1130/G35010.1>
- Choukroun, M., O'Reilly, S. Y., Griffin, W. L., Pearson, N. J., & Dawson, J. B. (2005). Hf isotopes of MARID (mica-amphibole-rutile-ilmenite-diopside) rutile trace metasomatic processes in the lithospheric mantle. *Geology*, 33(1), 45–48. <https://doi.org/10.1130/G21084.1>
- Conrad, C. P., & Molnar, P. (1997). The growth of Rayleigh-Taylor-type instabilities in the lithosphere for various rheological and density structures. *Geophysical Journal International*, 129(1), 95–112. <https://doi.org/10.1111/j.1365-246X.1997.tb00939.x>
- Dabrowski, M., Krotkiewski, M., & Schmid, D. W. (2008). MILAMIN: MATLAB-based finite element method solver for large problems. *Geochemistry, Geophysics, Geosystems*, 9, Q04030. <https://doi.org/10.1029/2007GC001719>
- Dalton, J. A., & Presnall, D. C. (1998). Carbonatitic melts along the solidus of model lherzolite in the system CaO-MgO-Al₂O₃-SiO₂-CO₂ from 3 to 7 GPa. *Contributions to Mineralogy and Petrology*, 131(2–3), 123–135. <https://doi.org/10.1007/s004100050383>
- Davis, G. A., Yadong, Z., Cong, W., Darby, B. J., Changhou, Z., & Gehrels, G. (2001). Mesozoic tectonic evolution of the Yanshan fold and thrust belt, with emphasis on Hebei and Liaoning provinces, northern China. *Memoir - Geological Society of America*, 171–198.
- Dawson, J. B., & Smith, J. (1988). Metasomatised and veined upper-mantle xenoliths from Pello Hill, Tanzania: Evidence for anomalously-light mantle beneath the Tanzanian sector of the East African Rift Valley. *Contributions to Mineralogy and Petrology*, 100(4), 510–527. <https://doi.org/10.1007/BF00371380>
- Dawson, J. B., & Smith, J. V. (1977). The MARID (mica-amphibole-rutile-ilmenite-diopside) suite of xenoliths in kimberlite. *Geochimica et Cosmochimica Acta*, 41(2), 309–310.
- Dimanov, A., Lavie, M. P., Dresen, G., Ingrin, J., & Jaoul, O. (2003). Creep of polycrystalline anorthite and diopside. *Journal of Geophysical Research*, 108(B1), 2061. <https://doi.org/10.1029/2002JB001815>
- Djomani, Y. H. P., O'Reilly, S. Y., Griffin, W. L., & Morgan, P. (2001). The density structure of subcontinental lithosphere through time. *Earth and Planetary Science Letters*, 184(3–4), 605–621. [https://doi.org/10.1016/S0012-821X\(00\)00362-9](https://doi.org/10.1016/S0012-821X(00)00362-9)
- Downes, H., MacDonald, R., Upton, B. G. J., Cox, K. G., Bodinier, J. L., Mason, P. R. D., et al. (2004). Ultramafic xenoliths from the Bearpaw Mountains, Montana, USA: Evidence for multiple metasomatic events in the lithospheric mantle beneath the Wyoming craton. *Journal of Petrology*, 45(8), 1631–1662. <https://doi.org/10.1093/petrology/egh027>
- Dudás, F. Ö. (1991). Geochemistry of igneous rocks from the Crazy Mountains, Montana, and tectonic models for the Montana alkalic province. *Journal of Geophysical Research*, 96(B8), 13,261–13,277. <https://doi.org/10.1029/91JB00246>
- Dudás, F. Ö., Ispolatov, V. O., Harlan, S. S., & Snee, L. W. (2010). 40Ar/39Ar geochronology and geochemical reconnaissance of the Eocene Lowland Creek volcanic field, west-central Montana. *The Journal of Geology*, 118(3), 295–304. <https://doi.org/10.1086/651523>
- Eggler, D., & Furlong, K. (1991). Destruction of subcratonic mantle keel: The Wyoming Province. Proceedings of the 5. International Kimberlite Conference - Extended abstracts, CPRM Special Publication 2/91, Rio de Janeiro, Brazil (1991), 85–87
- Eggler, D. H. (1978). The effect. *American Journal of Science*, 278(3), 305–343. <https://doi.org/10.2475/ajs.278.3.305>
- Engelbreton, D. C., Cox, A., & Gordon, R. G. (1985). Relative motions between oceanic and continental plates in the Pacific basin. *Geological Society of America Special Papers*, 206, 1–60. <https://doi.org/10.1130/SPE206-p1>
- English, J. M., & Johnston, S. T. (2004). The Laramide orogeny: What were the driving forces? *International Geology Review*, 46(9), 833–838. <https://doi.org/10.2747/0020-6814.46.9.833>
- Faccenna, C., Funicello, F., Giardini, D., & Lucente, P. (2001). Episodic back-arc extension during restricted mantle convection in the Central Mediterranean. *Earth and Planetary Science Letters*, 187(1–2), 105–116. [https://doi.org/10.1016/S0012-821X\(01\)00280-1](https://doi.org/10.1016/S0012-821X(01)00280-1)
- Feeley, T. C., & Cosca, M. A. (2003). Time vs. composition trends of magmatism at Sunlight volcano, Absaroka volcanic province, Wyoming. *Geological Society of America Bulletin*, 115(6), 714–728. [https://doi.org/10.1130/0016-7606\(2003\)115<0714:Tvctom>2.0.Co;2](https://doi.org/10.1130/0016-7606(2003)115<0714:Tvctom>2.0.Co;2)
- Feeley, T. C., Cosca, M. A., & Lindsay, C. R. (2002). Petrogenesis and implications of calc-alkaline cryptic hybrid magmas from Washburn volcano, Absaroka Volcanic Province, USA. *Journal of Petrology*, 43(4), 663–703. <https://doi.org/10.1093/petrology/43.4.663>
- Foley, S. F. (2008). Rejuvenation and erosion of the cratonic lithosphere. *Nature Geoscience*, 1(8), 503–510. <https://doi.org/10.1038/ngeo261>
- Foster, D. A., Mueller, P. A., Heatherington, A., Gifford, J. N., & Kalakay, T. J. (2012). Lu-Hf systematics of magmatic zircons reveal a Proterozoic crustal boundary under the Cretaceous Pioneer batholith, Montana. *Lithos*, 142–143, 216–225. <https://doi.org/10.1016/j.lithos.2012.03.005>
- Foster, D. A., Mueller, P. A., Mogk, D. W., Wooden, J. L., & Vogl, J. J. (2006). Proterozoic evolution of the western margin of the Wyoming craton: Implications for the tectonic and magmatic evolution of the northern Rocky Mountains. *Canadian Journal of Earth Sciences*, 43(10), 1601–1619. <https://doi.org/10.1139/E06-052>
- Francis, D. F., Minarik, W. M., Proenza, Y. P., & Shi, L. S. (2010). An overview of the Canadian Cordilleran lithospheric mantle. This article. *Canadian Journal of Earth Sciences*, 47(4), 353–368. <https://doi.org/10.1139/E09-072>
- Gao, S., Rudnick, R. L., Carlson, R. W., McDonough, W. F., & Liu, Y. S. (2002). Re-Os evidence for replacement of ancient mantle lithosphere beneath the North China craton. *Earth and Planetary Science Letters*, 198(3–4), 307–322. [https://doi.org/10.1016/S0012-821X\(02\)00489-2](https://doi.org/10.1016/S0012-821X(02)00489-2)
- Gao, S., Zhang, J. F., Xu, W. L., & Liu, Y. S. (2009). Delamination and destruction of the North China Craton. *Chinese Science Bulletin*, 54(19), 3367–3378. <https://doi.org/10.1007/s11434-009-0395-9>

- Gaschnig, R. M., Vervoort, J. D., Lewis, R. S., & McClelland, W. C. (2010). Migrating magmatism in the northern US Cordillera: In situ U-Pb geochronology of the Idaho batholith. *Contributions to Mineralogy and Petrology*, 159(6), 863–883. <https://doi.org/10.1007/s00410-009-0459-5>
- Getsinger, A. J., & Hirth, G. (2014). Amphibole fabric formation during diffusion creep and the rheology of shear zones. *Geology*, 42(6), 535–538. <https://doi.org/10.1130/G35327.1>
- Gorczyk, W., Hobbs, B., & Gerya, T. (2012). Initiation of Rayleigh-Taylor instabilities in intra-cratonic settings. *Tectonophysics*, 514–517, 146–155. <https://doi.org/10.1016/j.tecto.2011.10.016>
- Gray, R., & Pysklywec, R. N. (2012). Geodynamic models of mature continental collision: Evolution of an orogen from lithospheric subduction to continental retreat/delamination. *Journal of Geophysical Research*, 117, B03408. <https://doi.org/10.1029/2011JB008692>
- Griffin, W. L., Andi, Z., O'Reilly, S. Y., & Ryan, C. G. (1998). Phanerozoic evolution of the lithosphere beneath the Sino-Korean Craton. *Mantle Dynamics and Plate Interactions in East Asia*, 27, 107–126. <https://doi.org/10.1029/GD027p0107>
- Griffin, W. L., Batumike, J. M., Greau, Y., Pearson, N. J., Shee, S. R., & O'Reilly, S. Y. (2014). Emplacement ages and sources of kimberlites and related rocks in southern Africa: U-Pb ages and Sr-Nd isotopes of groundmass perovskite. *Contributions to Mineralogy and Petrology*, 168(1), 1–13. <https://doi.org/10.1007/S00410-014-1032-4>
- Griffin, W. L., Kobussen, A. F., Babu, E. V. S. S. K., O'Reilly, S. Y., Norris, R., & Sengupta, P. (2009). A trans-lithospheric suture in the vanished 1-Ga lithospheric root of South India: Evidence from contrasting lithosphere sections in the Dharwar Craton. *Lithos*, 112, 1109–1119. <https://doi.org/10.1016/j.lithos.2009.05.015>
- Griffin, W. L., O'Reilly, S. Y., Afonso, J. C., & Begg, G. C. (2009). The composition and evolution of lithospheric mantle: A re-evaluation and its tectonic implications. *Journal of Petrology*, 50(7), 1185–1204. <https://doi.org/10.1093/petrology/egn033>
- Griffin, W. L., O'Reilly, S. Y., Doyle, B. J., Pearson, N. J., Coopersmith, H., Kivi, K., et al. (2004). Lithosphere mapping beneath the north American plate. *Lithos*, 77(1–4), 873–922. <https://doi.org/10.1016/j.lithos.2004.03.034>
- Griffin, W. L., O'Reilly, S. Y., Natapov, L. M., & Ryan, C. G. (2003). The evolution of lithospheric mantle beneath the Kalahari Craton and its margins. *Lithos*, 71(2–4), 215–241. <https://doi.org/10.1016/j.lithos.2003.07.006>
- Griffin, W. L., O'Reilly, S. Y., & Ryan, C. G. (1999). The composition and origin of subcontinental lithospheric mantle. In Y. Fei, C. M. Bertka, & B. O. Mysen (Eds.), *Mantle petrology: Field observation and high pressure experimentation: A tribute to Francis R. (Joe) Boyd*, *Geochemical Society Special Publication* (Vol. 6, pp. 13–45).
- Hansen, S. M., Dueker, K., & Schmandt, B. (2015). Thermal classification of lithospheric discontinuities beneath USArray. *Earth and Planetary Science Letters*, 431, 36–47. <https://doi.org/10.1016/j.epsl.2015.09.009>
- Hasenclever, J. (2010). Modeling mantle flow and melting processes at mid-ocean ridges and subduction zones—Development and application of numerical models. Ph.D. Dissertation, Hamburg University. URL: <http://ediss.sub.uni-hamburg.de/volltexte/2010/4873/>.
- Hasenclever, J., Morgan, J. P., Hort, M., & Rupke, L. H. (2011). 2D and 3D numerical models on compositionally buoyant diapirs in the mantle wedge. *Earth and Planetary Science Letters*, 311(1–2), 53–68. <https://doi.org/10.1016/j.epsl.2011.08.043>
- He, D., Dong, S., Santosh, M., Li, Q., & Chen, X. (2015). Destruction of the North China Craton: A perspective based on receiver function analysis. *Geological Journal*, 50(1), 93–103. <https://doi.org/10.1002/gj.2530>
- He, L. J. (2014). Numerical modeling of convective erosion and peridotite-melt interaction in big mantle wedge: Implications for the destruction of the North China Craton. *Journal of Geophysical Research: Solid Earth*, 119, 3662–3677. <https://doi.org/10.1002/2013JB010657>
- Hirschmann, M. M., Tenner, T., Aubaud, C., & Withers, A. C. (2009). Dehydration melting of nominally anhydrous mantle: The primacy of partitioning. *Physics of the Earth and Planetary Interiors*, 176(1–2), 54–68. <https://doi.org/10.1016/j.pepi.2009.04.001>
- Hirth, G., & Kohlstedt, D. (2004). Rheology of the upper mantle and the mantle wedge: A view from the experimentalists. In J. Eiler (Ed.), *Inside the subduction factory* (Vol. 138, pp. 83–105). Washington, DC: American Geophysical Union. <https://doi.org/10.1029/138GM06>
- Hirth, G., & Kohlstedt, D. L. (1995). Experimental constraints on the dynamics of the partially molten upper-mantle - deformation in the diffusion creep regime. *Journal of Geophysical Research*, 100(B2), 1981–2001. <https://doi.org/10.1029/94JB02128>
- Hirth, G., & Kohlstedt, D. L. (1996). Water in the oceanic upper mantle: Implications for rheology, melt extraction and the evolution of the lithosphere. *Earth and Planetary Science Letters*, 144(1–2), 93–108. [https://doi.org/10.1016/0012-821x\(96\)00154-9](https://doi.org/10.1016/0012-821x(96)00154-9)
- Hopper, E., Ford, H. A., Fischer, K. M., Lekic, V., & Fouch, M. J. (2014). The lithosphere-asthenosphere boundary and the tectonic and magmatic history of the northwestern United States. *Earth and Planetary Science Letters*, 402, 69–81. <https://doi.org/10.1016/j.epsl.2013.12.016>
- Houseman, G. A., McKenzie, D. P., & Molnar, P. (1981). Convective instability of a thickened boundary-layer and its relevance for the thermal evolution of continental convergent belts. *Journal of Geophysical Research*, 86(Nb7), 6115–6132. <https://doi.org/10.1029/Jb086ib07p06115>
- Jordan, T. H. (1988). Structure and formation of the continental tectosphere. *Journal of Petrology*, 1, 11–37.
- Kaban, M. K., Schwintzer, P., Artemieva, I. M., & Mooney, W. D. (2003). Density of the continental roots: Compositional and thermal contributions. *Earth and Planetary Science Letters*, 209(1–2), 53–69. [https://doi.org/10.1016/S0012-821x\(03\)00072-4](https://doi.org/10.1016/S0012-821x(03)00072-4)
- Kaban, M. K., Stolk, W., Tesauro, M., El Khrepy, S., Al-Arifi, N., Beekman, F., & Cloetingh, S. A. P. L. (2016). 3D density model of the upper mantle of Asia based on inversion of gravity and seismic tomography data. *Geochemistry, Geophysics, Geosystems*, 17, 4457–4477. <https://doi.org/10.1002/2016GC006458>
- Karato, S., & Wu, P. (1993). Rheology of the upper mantle: A synthesis. *Science*, 260(5109), 771–778. <https://doi.org/10.1126/science.260.5109.771>
- Karato, S. I., Ologboji, T., & Park, J. (2015). Mechanisms and geologic significance of the mid-lithosphere discontinuity in the continents. *Nature Geoscience*, 8(7), 509–514. <https://doi.org/10.1038/NGEO2462>
- Katz, R. F., Spiegelman, M., & Langmuir, C. H. (2003). A new parameterization of hydrous mantle melting. *Geochemistry, Geophysics, Geosystems*, 4(9), 1073. <https://doi.org/10.1029/2002GC000433>
- Kaus, B. J. P., Muhlhaus, H., & May, D. A. (2010). A stabilization algorithm for geodynamic numerical simulations with a free surface. *Physics of the Earth and Planetary Interiors*, 181(1–2), 12–20. <https://doi.org/10.1016/j.pepi.2010.04.007>
- Kay, R. W., & Kay, S. M. (1993). Delamination and delamination magmatism. *Tectonophysics*, 219(1–3), 177–189. [https://doi.org/10.1016/0040-1951\(93\)90295-U](https://doi.org/10.1016/0040-1951(93)90295-U)
- Kay, S. M., & Coira, B. L. (2009). Shallowing and steepening subduction zones, continental lithospheric loss, magmatism, and crustal flow under the Central Andean Altiplano-Puna Plateau. *Geological Society of America Memoirs*, 204(0), 229–259. [https://doi.org/10.1130/2009.1204\(11\)](https://doi.org/10.1130/2009.1204(11))
- Kinck, J. J., Husebye, E. S., & Larsson, F. R. (1993). The Moho depth distribution in Fennoscandia and the regional tectonic evolution from Archean to Permian times. *Precambrian Research*, 64(1–4), 23–51. [https://doi.org/10.1016/0301-9268\(93\)90067-C](https://doi.org/10.1016/0301-9268(93)90067-C)
- Kirby, S. H., & Kronenberg, A. K. (1987). Rheology of the lithosphere—Selected topics. *Reviews of Geophysics*, 25(6), 1219–1244. <https://doi.org/10.1029/RG025i006p01219>

- Korenaga, J., & Karato, S. I. (2008). A new analysis of experimental data on olivine rheology. *Journal of Geophysical Research*, *113*, B02403. <https://doi.org/10.1029/2007JB005100>
- Krystowicz, N. J., & Currie, C. A. (2013). Crustal eclogitization and lithosphere delamination in orogens. *Earth and Planetary Science Letters*, *361*, 195–207. <https://doi.org/10.1016/j.epsl.2012.09.056>
- Lan, T. G., Fan, H. R., Santosh, M., Hu, F. F., Yang, K. F., Yang, Y. H., & Liu, Y. S. (2012). Early Jurassic high-K calc-alkaline and shoshonitic rocks from the Tongshi intrusive complex, eastern North China Craton: Implication for crust-mantle interaction and post-collisional magmatism. *Lithos*, *140–141*, 183–199. <https://doi.org/10.1016/j.lithos.2012.01.015>
- Lee, C. T. A. (2003). Compositional variation of density and seismic velocities in natural peridotites at STP conditions: Implications for seismic imaging of compositional heterogeneities in the upper mantle. *Journal of Geophysical Research*, *108*(B9), 2441. <https://doi.org/10.1029/2003JB002413>
- Lee, C.-T. A., Luffi, P., & Chin, E. J. (2011). Building and destroying continental mantle. *Annual Review of Earth and Planetary Sciences*, *39*(1), 59–90. <https://doi.org/10.1146/annurev-earth-040610-133505>
- Lekić, V., & Fischer, K. M. (2014). Contrasting lithospheric signatures across the western United States revealed by Sp receiver functions. *Earth and Planetary Science Letters*, *402*, 90–98. <https://doi.org/10.1016/j.epsl.2013.11.026>
- Lenardic, A., & Moresi, L.-N. (1999). Some thoughts on the stability of cratonic lithosphere: Effects of buoyancy and viscosity. *Journal of Geophysical Research*, *104*(B6), 12,747–12,758. <https://doi.org/10.1029/1999JB900035>
- Li, H.-Y., Xu, Y.-G., Liu, Y.-M., Huang, X.-L., & He, B. (2013). Detrital zircons reveal no Jurassic plateau in the eastern North China Craton. *Gondwana Research*, *24*(2), 622–634. <https://doi.org/10.1016/j.gr.2012.12.007>
- Li, Z. H., Liu, M. A., & Gerya, T. (2016). Lithosphere delamination in continental collisional orogens: A systematic numerical study. *Journal of Geophysical Research: Solid Earth*, *121*, 5186–5211. <https://doi.org/10.1002/2016JB013106>
- Liu, L., Morgan, J., Xu, Y., and Menzies, M. (2016). Numerical modelling of the destruction of the Eastern North China Craton, paper presented at AGU Fall Meeting Abstracts, Abstract T11B-2624.
- Liu, L., Morgan, J., Xu, Y., Menzies, M. (2018). Craton Destruction 2: Evolution of cratonic lithosphere after a rapid keel delamination event. *Journal of Geophysical Research: Solid Earth*, *123*, 10,069–10,090. <https://doi.org/10.1029/2017JB015372>
- Lu, F., Han, Z., Zheng, J., & Ren, Y. (1991). Characteristics of Paleozoic mantle-lithosphere in Fuxian, Liaoning province. *Geological Science and Technology Information*, *10*, 2–19.
- Lund, K., Aleinikoff, J. N., Kunk, M. J., Unruh, D. M., Zeihen, G. D., Hodges, W. C., et al. (2002). SHRIMP U-Pb and ⁴⁰Ar/³⁹Ar age constraints for relating plutonism and mineralization in the Boulder Batholith region, Montana. *Economic Geology*, *97*(2), 241–267. <https://doi.org/10.2113/gsecongeo.97.2.241>
- Malkovets, V. G., Griffin, W. L., O'Reilly, S. Y., & Wood, B. J. (2007). Diamond, subcalcic garnet, and mantle metasomatism: Kimberlite sampling patterns define the link. *Geology*, *35*(4), 339. <https://doi.org/10.1130/G23092A.1>
- Malvern, L. E. (1969). *Introduction to the mechanics of a continuous medium* (p. 713). Englewood Cliffs, NJ: Prentice-Hall, Inc.
- Manea, V. C., Perez-Gussinye, M., & Manea, M. (2012). Chilean flat slab subduction controlled by overriding plate thickness and trench roll-back. *Geology*, *40*(1), 35–38. <https://doi.org/10.1130/G32543.1>
- Maruyama, S., Isozaki, Y., Kimura, G., & Terabayashi, M. (1997). Paleogeographic maps of the Japanese Islands: Plate tectonic synthesis from 750 Ma to the present. *Island Arc*, *6*(1), 121–142. <https://doi.org/10.1111/j.1440-1738.1997.tb00043.x>
- Menzies, M., Xu, Y. G., Zhang, H. F., & Fan, W. M. (2007). Integration of geology, geophysics and geochemistry: A key to understanding the North China Craton. *Lithos*, *96*(1–2), 1–21. <https://doi.org/10.1016/j.lithos.2006.09.008>
- Menzies, M., Fan, W., & Zhang, M. (1993). Palaeozoic and Cenozoic lithoprobes and the loss of > 120 km of Archaean lithosphere, Sino-Korean craton, China. *Geological Society, London, Special Publications*, *76*(1), 71–81. <https://doi.org/10.1144/GSL.SP.1993.076.01.04>
- Mooney, W. D., & Kaban, M. K. (2010). The North American upper mantle: Density, composition, and evolution. *Journal of Geophysical Research*, *115*, B12424. <https://doi.org/10.1029/2010JB000866>
- Morency, C., & Doin, M. P. (2004). Numerical simulations of the mantle lithosphere delamination. *Journal of Geophysical Research*, *109*, B03410. <https://doi.org/10.1029/2003JB002414>
- Moresi, L., Dufour, F., & Muhlhaus, H. B. (2003). A Lagrangian integration point finite element method for large deformation modeling of viscoelastic geomaterials. *Journal of Computational Physics*, *184*(2), 476–497. [https://doi.org/10.1016/S0021-9991\(02\)00031-1](https://doi.org/10.1016/S0021-9991(02)00031-1)
- Morgan, J. P. (2001). Thermodynamics of pressure release melting of a veined plum pudding mantle. *Geochemistry, Geophysics, Geosystems*, *2*(4), 1001. <https://doi.org/10.1029/2000GC000049>
- Mueller, P., Heatherington, A., D'Arcy, K., Wooden, J., & Nutman, A. (1996). Contrasts between Sm-Nd whole-rock and U-Pb zircon systematics in the Tobacco Root batholith, Montana: Implications for the determination of crustal age provinces. *Tectonophysics*, *265*(1–2), 169–179. [https://doi.org/10.1016/S0040-1951\(96\)00151-5](https://doi.org/10.1016/S0040-1951(96)00151-5)
- Nita, B., Maurya, S., & Montagner, J. P. (2016). Anisotropic tomography of the European lithospheric structure from surface wave studies. *Geochemistry, Geophysics, Geosystems*, *17*, 2015–2033. <https://doi.org/10.1002/2015GC006243>
- Niu, Y. (2005). Generation and evolution of basaltic magmas: Some basic concepts and a new view on the origin of Mesozoic–Cenozoic basaltic volcanism in eastern China. *Geological Journal of China Universities*, *11*(1), 9–46.
- Norman, M. D., & Mertzman, S. A. (1991). Petrogenesis of Challis Volcanics from Central and Southwestern Idaho—Trace-element and Pb isotopic evidence. *Journal of Geophysical Research*, *96*(B8), 13,279–13,293. <https://doi.org/10.1029/91JB00285>
- O'Reilly, S. Y., & Griffin, W. (2013). Mantle metasomatism. In D. E. Harlov & H. Austrheim (Eds.), *Metasomatism and the chemical transformation of rock: the role of fluids in terrestrial and extraterrestrial processes* (pp. 471–533). Heidelberg, London: Springer.
- O'Reilly, S. Y., Griffin, W., Poudjom Djomani, Y., & Morgan, P. (2001). Are lithospheres forever, tracking changes in subcontinental lithospheric mantle through time. *GSA Today*, *11*(4), 4–10.
- Parmentier, E., & Forsyth, D. (1985). Three-dimensional flow beneath a slow spreading ridge axis: A dynamic contribution to the deepening of the median valley toward fracture zones. *Journal of Geophysical Research*, *90*(B1), 678–684. <https://doi.org/10.1029/JB090iB01p00678>
- Persson, P. O., & Strang, G. (2004). A simple mesh generator in MATLAB. *SIAM Review*, *46*(2), 329–345. <https://doi.org/10.1137/S0036144503429121>
- Peslier, A. H., Reisberg, L., Ludden, J., & Francis, D. (2000). Os isotopic systematics in mantle xenoliths; age constraints on the Canadian Cordillera lithosphere. *Chemical Geology*, *166*(1–2), 85–101. [https://doi.org/10.1016/S0009-2541\(99\)00187-4](https://doi.org/10.1016/S0009-2541(99)00187-4)
- Précigout, J., Gueydan, F., Gapais, D., Garrido, C., & Essaifi, A. (2007). Strain localisation in the subcontinental mantle—A ductile alternative to the brittle mantle. *Tectonophysics*, *445*(3–4), 318–336. <https://doi.org/10.1016/j.tecto.2007.09.002>
- Read, G., Grutter, H., Winter, S., Luckman, N., Gaunt, F., & Thomsen, F. (2004). Stratigraphic relations, kimberlite emplacement and lithospheric thermal evolution, Quirico basin, Minas Gerais state, Brazil. *Lithos*, *77*(1–4), 803–818. <https://doi.org/10.1016/j.lithos.2004.04.011>

- Rybacki, E., & Dresen, G. (2004). Deformation mechanism maps for feldspar rocks. *Tectonophysics*, 382(3–4), 173–187. <https://doi.org/10.1016/j.tecto.2004.01.006>
- Schmeling, H., Babeyko, A., Enns, A., Faccenna, C., Funicello, F., Gerya, T., et al. (2008). A benchmark comparison of spontaneous subduction models—Towards a free surface. *Physics of the Earth and Planetary Interiors*, 171(1–4), 198–223. <https://doi.org/10.1016/j.pepi.2008.06.028>
- Schutt, D. L., & Leshner, C. E. (2006). Effects of melt depletion on the density and seismic velocity of garnet and spinel Ilherzolite. *Journal of Geophysical Research*, 111, B05401. <https://doi.org/10.1029/2003JB002950>
- Selway, K., Ford, H., & Kelemen, P. (2015). The seismic mid-lithosphere discontinuity. *Earth and Planetary Science Letters*, 414, 45–57. <https://doi.org/10.1016/j.epsl.2014.12.029>
- Sigloch, K., McQuarrie, N., & Nolet, G. (2008). Two-stage subduction history under North America inferred from multiple-frequency tomography. *Nature Geoscience*, 1(7), 458–462. <https://doi.org/10.1038/ngeo231>
- Sleep, N. H. (2003). Survival of Archean cratonic lithosphere. *Journal of Geophysical Research*, 108(B6), 2302. <https://doi.org/10.1029/2001JB000169>
- Sleep, N. H. (2009). Stagnant lid convection and carbonate metasomatism of the deep continental lithosphere. *Geochemistry, Geophysics, Geosystems*, 10, Q11010. <https://doi.org/10.1029/2009GC002702>
- Snyder, W., Dickinson, W., & Silberman, M. (1976). Tectonic implications of space-time patterns of Cenozoic magmatism in the western United States. *Earth and Planetary Science Letters*, 32(1), 91–106. [https://doi.org/10.1016/0012-821X\(76\)90189-8](https://doi.org/10.1016/0012-821X(76)90189-8)
- Sodoudi, F., Yuan, X. H., Kind, R., Lebedev, S., Adam, J. M. C., Kastle, E., & Tilmann, F. (2013). Seismic evidence for stratification in composition and anisotropic fabric within the thick lithosphere of Kalahari Craton. *Geochemistry, Geophysics, Geosystems*, 14, 5393–5412. <https://doi.org/10.1002/2013GC004955>
- Tang, Y. J., Zhang, H. F., Ying, J. F., & Su, B. X. (2013). Widespread refertilization of cratonic and circum-cratonic lithospheric mantle. *Earth-Science Reviews*, 118, 45–68. <https://doi.org/10.1016/j.earscirev.2013.01.004>
- Taramón, J. M., Morgan, J. P., Shi, C., & Hasenclever, J. (2017). Generation of unstructured meshes in 2-D, 3-D, and spherical geometries with embedded high resolution sub-regions; arXiv: 1711.06333.
- Tharimena, S., Rychert, C., & Harmon, N. (2017). A unified continental thickness from seismology and diamonds suggests a melt-defined plate. *Science*, 357(6351), 580–583. <https://doi.org/10.1126/science.aan0741>
- Tommasi, A., Knoll, M., Vauchez, A., Signorelli, J., Thoraval, C., & Loge, R. (2009). Structural reactivation in plate tectonics controlled by olivine crystal anisotropy. *Nature Geoscience*, 2(6), 423–427. <https://doi.org/10.1038/NGEO528>
- Turcotte, D. L., & Schubert, G. (2014). *Geodynamics* (p. 623). Cambridge, UK: Cambridge University Press. <https://doi.org/10.1017/CBO9780511843877>
- Wang, Z. S., Kusky, T. M., & Capitanio, F. A. (2016). Lithosphere thinning induced by slab penetration into a hydrous mantle transition zone. *Geophysical Research Letters*, 43, 11,567–11,577. <https://doi.org/10.1002/2016GL071186>
- Wenker, S., & Beaumont, C. (2017). Can metasomatic weakening result in the rifting of cratons? *Tectonophysics*, 0040-1951. <https://doi.org/10.1016/j.tecto.2017.06.013>
- Wilks, K. R., & Carter, N. L. (1990). Rheology of some continental lower crustal rocks. *Tectonophysics*, 182(1–2), 57–77. [https://doi.org/10.1016/0040-1951\(90\)90342-6](https://doi.org/10.1016/0040-1951(90)90342-6)
- Wu, F. Y., Sun, D. Y., Ge, W. C., Zhang, Y. B., Grant, M. L., Wilde, S. A., & Jahn, B. M. (2011). Geochronology of the Phanerozoic granitoids in northeastern China. *Journal of Asian Earth Sciences*, 41(1), 1–30. <https://doi.org/10.1016/j.jseas.2010.11.014>
- Wu, F. Y., Xu, Y. G., Zhu, R. X., & Zhang, G. W. (2014). Thinning and destruction of the cratonic lithosphere: A global perspective. *Science China Earth Sciences*, 57(12), 2878–2890. <https://doi.org/10.1007/s11430-014-4995-0>
- Wu, F. Y., Yang, J. H., Wilde, S. A., & Zhang, X. O. (2005). Geochronology, petrogenesis and tectonic implications of Jurassic granites in the Liaodong Peninsula, NE China. *Chemical Geology*, 221(1–2), 127–156. <https://doi.org/10.1016/j.chemgeo.2005.04.010>
- Xia, Q. K., Liu, J., Liu, S. C., Kovacs, I., Feng, M., & Dang, L. (2013). High water content in Mesozoic primitive basalts of the North China Craton and implications on the destruction of cratonic mantle lithosphere. *Earth and Planetary Science Letters*, 361, 85–97. <https://doi.org/10.1016/j.epsl.2012.11.024>
- Xiao, X., Wirth, R., & Dresen, G. (2002). Diffusion creep of anorthite-quartz aggregates. *Journal of Geophysical Research*, 107(B11), 2279. <https://doi.org/10.1029/2001JB000789>
- Xu, Y. G. (2001). Thermo-tectonic destruction of the Archaean lithospheric keel beneath the Sino-Korean Craton in China: Evidence, timing and mechanism. *Physics and Chemistry of the Earth, Part A*, 26(9–10), 747–757. [https://doi.org/10.1016/S1464-1895\(01\)00124-7](https://doi.org/10.1016/S1464-1895(01)00124-7)
- Xu, Y. G., Li, H. Y., Pang, C. J., & He, B. (2009). On the timing and duration of the destruction of the North China Craton. *Chinese Science Bulletin*, 54(19), 3379–3396. <https://doi.org/10.1007/s11434-009-0346-5>
- Yamamoto, M., Morgan, J. P., & Morgan, W. J. (2007). Global plume-fed asthenosphere flow—I: Motivation and model development. *Geological Society of America Special Papers*, 430, 165–188.
- Yang, K. F., Fan, H. R., Santosh, M., Hu, F. F., Wilde, S. A., Lan, T. G., et al. (2012). Reactivation of the Archean lower crust: Implications for zircon geochronology, elemental and Sr-Nd-Hf isotopic geochemistry of late Mesozoic granitoids from northwestern Jiaodong Terrane, the North China Craton. *Lithos*, 146–147, 112–127. <https://doi.org/10.1016/j.lithos.2012.04.035>
- Yang, W., & Li, S. G. (2008). Geochronology and geochemistry of the Mesozoic volcanic rocks in Western Liaoning: Implications for lithospheric thinning of the North China Craton. *Lithos*, 102(1–2), 88–117. <https://doi.org/10.1016/j.lithos.2007.09.018>
- Youssef, M., Thybo, H., Artemieva, I. M., & Levander, A. (2013). Moho depth and crustal composition in Southern Africa. *Tectonophysics*, 609, 267–287. <https://doi.org/10.1016/j.tecto.2013.09.001>
- Zhang, H. F., Goldstein, S. L., Zhou, X. H., Sun, M., Zheng, J. P., & Cai, Y. (2008). Evolution of s ubcontinental lithospheric mantle beneath eastern China: Re-Os isotopic evidence from mantle xenoliths in Paleozoic kimberlites and Mesozoic basalts. *Contributions to Mineralogy and Petrology*, 155(3), 271–293. <https://doi.org/10.1007/s00410-007-0241-5>
- Zhao, D. P. (2004). Global tomographic images of mantle plumes and subducting slabs: Insight into deep Earth dynamics. *Physics of the Earth and Planetary Interiors*, 146(1–2), 3–34. <https://doi.org/10.1016/j.pepi.2003.07.032>
- Zhao, Y., Song, B., & Zhang, S. (2006). Geochronology of the inherited zircons from Jurassic Nandaling basalt of the Western Hills of Beijing, North China: Its implications. *Earth Science Frontiers*, 13(2), 184–190.
- Zheng, J. P., Griffin, W. L., O'Reilly, S. Y., Hu, B. Q., Zhang, M., Tang, H. Y., et al. (2008). Continental collision and accretion recorded in the deep lithosphere of Central China. *Earth and Planetary Science Letters*, 269(3–4), 497–507. <https://doi.org/10.1016/j.epsl.2008.03.003>
- Zheng, J. P., O'Reilly, S. Y., Griffin, W. L., Lu, F. X., Zhang, M., & Pearson, N. J. (2001). Relict refractory mantle beneath the eastern North China block: Significance for lithosphere evolution. *Lithos*, 57(1), 43–66. [https://doi.org/10.1016/S0024-4937\(00\)00073-6](https://doi.org/10.1016/S0024-4937(00)00073-6)
- Zhu, Y., Xu, G., Zhu, H., Zhang, H., Xia, Q., & Zheng, T. (2012). Destruction of the North China Craton. *Science China Earth Sciences*, 55(10), 1565–1587. <https://doi.org/10.1007/s11430-012-4516-y>